ASSESSMENT OF BRAIN PERFUSION AND VASCULAR COMPLIANCE

WITH MAGNETIC RESONANCE IMAGING

APPROVED BY SUPERVISORY COMMITTEE

Hanzhang Lu, Ph.D. (Mentor)
Elena Vinogradov. Ph.D.
Changho Choi, Ph.D.
Hanli Liu, Ph.D.
Ty Shang, M.D., Ph.D.

DEDICATION

To my advisor, Dr. Hanzhang Lu, who welcomed me to the field of MRI and influenced me tremendously as a great scientist.

To my parents, Shumei and Shichen, who are always there for me and support me unconditionally.

To my wife, Lili, your love has brightened my life.

ASSESSMENT OF BRAIN PERFUSION AND VASCULAR COMPLIANCE WITH MAGNETIC RESONANCE IMAGING

by

YANG LI

DISSERTATION

Presented to the Faculty of the Graduate School of Biomedical Sciences

The University of Texas Southwestern Medical Center at Dallas

In Partial Fulfillment of the Requirements

For the Degree of

DOCTOR OF PHILOSOPHY

The University of Texas Southwestern Medical Center at Dallas

Dallas, Texas

May, 2018

ASSESSMENT OF BRAIN PERFUSION AND VASCULAR COMPLIANCE WITH MAGNETIC RESONANCE IMAGING

Publication No. _____

Yang Li, Ph.D.

The University of Texas Southwestern Medical Center at Dallas, 2018

Supervising Professor: Hanzhang Lu, Ph.D.

Brain perfusion is an index that reflects the amount of blood received by the brain tissue in a given time period. Normal brain perfusion ensures that sufficient oxygen, glucose, and other nutrients are delivered to the neurons and glial cells in the brain. While perfusion is relatively static index of brain vascular function, vascular compliance represents the dynamic ability of arteries to dilate or retract in response to blood pressure alternations. An artery vessel with high compliance can better buffer the pulsatility of blood flow, thereby protecting the downstream arterioles and capillaries from damage.

Consequently, brain perfusion and vascular compliance are complementary properties of brain's vascular system and may be important indicators of cerebrovascular health. Therefore, noninvasive imaging of brain perfusion and vascular compliance will provide valuable biomarkers to study cerebral physiology and function. Furthermore, these biomarkers may also yield crucial pathophysiological knowledge and guide therapies in brain disorders, such as stroke, small-vessel disease, and neurodegenerative disease. This thesis consists of three novel tools toward brain perfusion and vascular compliance imaging. I first developed a cardiac-triggered Arterial-Spin-Labeling (ASL) technique to enhance the sensitivity of brain perfusion MRI without using exogenous contrast agent. I demonstrated its utility in several experimental settings, including single-shot acquisition, multi-shot acquisition, and detection of cerebral blood flow (CBF) changes. Next, I worked on the analysis strategies of perfusion MRI data. I developed a cloud-based tool for ASL data processing that is free from any software installation, compatible with file formats from all major MRI manufacturers, and publicly accessible. Quantitative CBF maps and region-specific reports are available for download within minutes. I have launched this cloud service recently and received initial feedback from researchers around the world. Finally, I developed a technique to measure vascular compliance in larger cerebral arteries. I used a time-resolved vascular-space-occupancy technique to obtain 3D maps of cerebral arterial compliance and then applied the technique to study arterial stiffness in aging.

TABLE OF CONTENTS

PRIOR PUBLICATIONS

1. **Li Y**, Mao D, Pillai JJ, Lu H. Non-contrast vascular compliance mapping using time-resolved VASO CBV imaging. (In preparation).

2. **Li Y**, Liu P, Li Y, Fan H, Su P, Peng SL, Park CD, Rodrigue MK, Jiang H, Faria VA, Ceritoglu C, Miller M, Mori S, Lu H. ASL-MRICloud: an online tool for the processing of ASL MRI data. (In preparation).

3. Peng SL, Chen X, **Li Y**, Rodrigue K, Park D, Lu H, Age-related decline in cerebrovascular function predicts cognition: a four-year longitudinal study. (In revision).

4. Lin Z, **Li Y**, Su P, Mao D, Wei Z, Pillai JJ, Moghekar A, van Osch M, Ge Y, Lu H. Non-contrast assessment of blood-brain-barrier permeability with MRI. Magn Reson Med 2018 (In-press).

5. **Li Y**, Mao D, Pillai JJ, Li Z, Shar M, Pipe GJ, Lu H. Cardiac-triggered pCASL: A cost-effective scheme to further enhance the reliability of ASL MRI. Magn Reson Med 2018 Jan 25. doi: 10.1002/mrm.27090. [Epub ahead of print]

6. Jiang D, Liu P, **Li Y**, Mao D, Xu C, Lu H. Cross-vendor harmonization of T2-Relaxation-Under-Spin-Tagging (TRUST) MRI for the assessment of cerebral venous oxygenation. Magn Reson Med 2018 Jan 25. doi: 10.1002/mrm.27080. [Epub ahead of print]

7. De Vis BJ, Peng SL, Chen X, **Li Y**, Liu P, Sur S, Rodrigue MK, Park CD, Lu H. Arterial-Spin-Labeling (ASL) perfusion MRI can predict cognitive function in elderly individuals: a four-year longitudinal study. J Magn Reson Imag 2018 Jan 2. doi: 10.1002/jmri.25938. [Epub ahead of print]

8. Mao D, **Li Y**, Liu P, Peng SL, Pillai JJ, Lu H. Three-dimensional mapping of brain venous oxygenation using R2* oximetry. Magn Reson Med 2018;79(3):1304-1313.

9. Sheng M, Lu HZ, Liu PY, **Li Y**, Ravi H, Peng SL, Diaz-Arrastia R, Devous MD, Womack KB. Sildenafil Improves Vascular and Metabolic Function in Patients with Alzheimer's Disease. J Alzheimers Dis 2017;60(4):1351-1364.

10. Su P, Mao D, Liu P, **Li Y**, Pinho MC, Welch BG, Lu H. Multiparametric estimation of brain hemodynamics with MR fingerprinting ASL. Magn Reson Med 2017;78(5):1812-1823.

11. Liu P, Welch BG, **Li Y**, Gu H, King D, Yang Y, Pinho M, Lu H. Multiparametric imaging of brain hemodynamics and function using gas-inhalation MRI. Neuroimage 2017;146:715-723.

12. Liu P, **Li Y**, Pinho M, Park DC, Welch BG, Lu H. Cerebrovascular reactivity mapping without gas challenges. Neuroimage 2017;146:320-326.

LIST OF FIGURES

LIST OF TABLES

LIST OF DEFINATIONS

ACA	Anterior Cerebral Artery
ASL	Arterial Spin Labeling
ATT	Arterial Travel Time
BIR	B1-Insensitive Rotation
BS	Background Suppression
CBF	Cerebral Blood Flood
CBV	Cerebral Blood Volume
CompCor	Component-based noise Correction method
CoV	Coefficient of variaiton
CSF	Cerebral Spinal Fluid
ECG	Electrocardiogram
FOCI	Frequency Offset Corrected Inversion
FOV	Field of View
GRASE	Gradient and Spin Echo
MCA	Middle Cerebral Artery
MNI	Montreal Neurologic Institute
MRI	Magnetic Resonance Imaging
PASL	Pulsed Arterial Spin Labeling
PCA	Posterior Cerebral Artery
PCASL	Pseudo-continuous Arterial Spin Labeling
PET	Positron Emission Tomography

PLD	Post-labeling delay
QI	Quality Index
RETROICOR	Image-based method for RETROspective CORrection
ROI	Region-of-Interest
SNR	Signal-to-Noise Ratio
TI	Inversion Time
TOF	Time of Flight
TR	Recovery Time
VASO	Vascular Space Occupancy
VC	Vascular Compliance

CHAPTER ONE

1 Introduction

1.1 Background

The healthy brain represents about 2% of the total body weight, but receives 15% of cardiac output under normal conditions (Gallagher et al 1998). Sufficient and steady blood supply to the neural tissue is vital to maintain normal brain functions. Brain perfusion is an index that reflects the amount of blood taken up by certain region of brain tissue within a time period (Young 1997). Normal brain perfusion ensures sufficient oxygen, glucose, and other nutrients are delivered to neurons and glial cells through capillary. While artery stiffness represents the ability of large arteries to dilate in response to blood pressure increase (Hademenos & Massoud 1998). An artery with high compliance (or low stiffness) can cushion the pulsatile blood flow from heart and thus protect the downstream arterioles from damage by pulsatile energy. Consequently, the brain perfusion and artery stiffness are two complementary properties of cerebrovascular system that covers the full spectrum of brain vessel caliber, from major arteries to capillary, offering important indicators of cerebrovascular health. Noninvasive imaging of brain perfusion as well as artery stiffness would provide valuable biomarkers to study cerebral physiology and function (Liang et al 2013, Tarumi et al 2014). On the other hand, these biomarkers can also enrich

pathophysiological knowledge and target therapies in brain disorders, such as stroke (Chalela et al 2000a, Zaharchuk et al 2012a), small-vessel disease (Henskens et al 2008, Poels et al 2012b), and neurodegenerative disorders (Alsop et al 2000, Hanon et al 2005).

1.1.1 Motives, strategies, and challenges in brain perfusion imaging

Brain perfusion imaging techniques provide essential information about hemodynamics in the brain (Wintermark et al 2005). As a result, they have enjoyed profound clinical applications in diagnosis of various disease conditions. For example, acute ischemic stroke is characterized by the sudden loss of blood circulation to an area of the brain due to occlusion of a cerebral artery (van der Worp & van Gijn 2007). The only FDA approved medication to treat such a disease is intravenous tissue plasminogen activator, but it has only been demonstrated to improve the condition within 5 hours of symptom onset in a limited portion of stroke patient (Clark et al 1999, Hacke et al 2008). Delayed intervention beyond time window of 5 hours is possible yet depends on the accurate detection of tissue area that is potentially recoverable (Astrup et al 1981, Heiss & Graf 1994).

As the gold standard in brain perfusion imaging, ^{15}O positron emission tomography (PET) has been proven to be capable of reliably identifying irreversible tissue dame and penumbra region (Baron et al 1981, Sobesky et al 2005). However, ^{15}O PET suffers from several limitations, including complexity (access to cyclotron PET radiopharmaceuticals), invasiveness (intravenous injection), and radiation exposure (radioactive tracers), which restricted its utilities in clinical settings (Wintermark et al 2005). Another less demanding MRI-based technique for perfusion imaging is dynamic susceptibility contrast (DSC) MRI. DSC relies on the fast measurement of the T2 decrease during the pass of an exogenous endovascular tracer through the capillary bed

(Wintermark et al 2005). The acquisition duration usually lasts around 1 minute and the patients are not exposed to ionizing radiation. When combined with diffusion-weighted imaging (DWI), the condition of stroke patients can be effectively evaluated and the subsequent treatment can be determined. But the technique in clinical practice still involves intravenous injection of gadolinium contrast-agent, which is invasive and may not feasible to patients with kidney disease (Kalb et al 2008).

Arterial spin labeling (ASL) perfusion MRI has emerged as a non-invasive technique for quantification of blood flow (Detre et al 1992, Williams et al 1992) by using the blood water as the endogenous diffusible tracer (see Figure 1.1). Briefly, a radiofrequency (RF) pulses was applied on the neck region such that the magnetization of incoming blood through the carotid artery is inverted. After a delay to allow for labeled blood to flow into the brain tissue, labeled images are acquired, containing signal from both labeled water and static tissue water. Separate control images are also acquired without labeling of incoming blood. Thus, the difference between control and label provides a measure of brain perfusion. When applied in acute ischemic stroke, ASL perfusion imaging can depicts perfusion deficits and perfusion/diffusion mismatches (Rohl et al 2001, Schlaug et al 1999), mentioned above as penumbra (see Figure 1.2). Besides stroke, ASL Perfusion imaging also plays an important role in several diseases that falls in the category of cerebrovascular diseases. For example, ASL perfusion imaging has been shown potentials to diagnose chronic occlusive disease of intracranial vessels, such as atherosclerosis (Gargiulo et al 2013) and Moyamoya disease (Zaharchuk et al 2011). Therefore, the development and optimization of ASL MRI technique is desirable to measure the perfusion reliably.

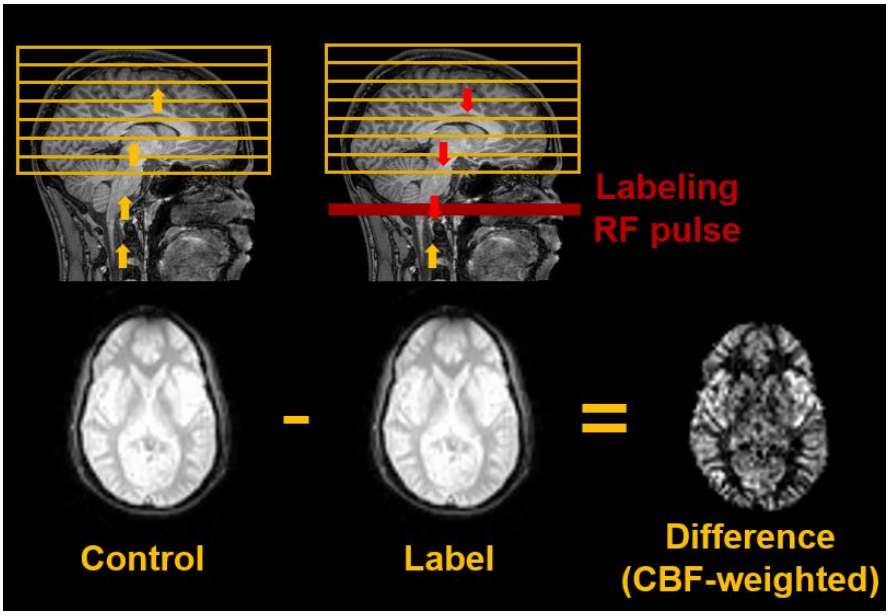

Figure 1.1 Schematic diagram of ASL technique to measure cerebral blood flow. Two images are acquired, one with RF-inverted incoming blood, one without. Followed by a short waiting time for the labeled blood to travel to the destination brain tissue, tissue signal cancels out after subtraction of the two images, leaving only signal from the labeled blood.

However, ASL technique suffers from its intrinsically low signal-to-noise ratio (SNR) due to the small volume fraction of perfused blood spins in the tissue, in which only ~1% of the relaxed brain signal is left after eliminating background tissue by pairwise subtraction between control and label images. Over the past decade of active development and evolving, several techniques have been invented and incorporated into ASL to improve the reliability of perfusion measurement. For example, a long post labeling delay is inserted between labeling module and acquisition such that there is no labeled blood remaining in the arteries to cause vascular artifacts (Alsop & Detre 1996). Background suppression (BS) is also introduced to decrease the signal intensity of unsubtracted images while preserve the difference signal (Garcia et al 2005, Ye et al 2000). The physiological

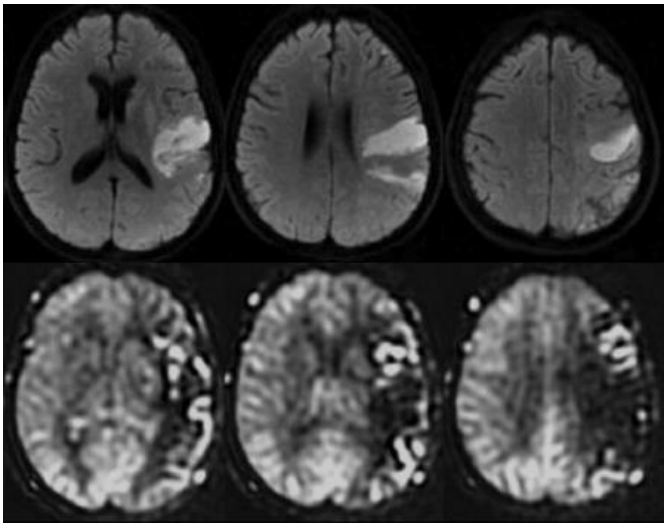

Figure 1.2 Diffusion/perfusion mismatch in acute stroke patient.
Top row shows the diffusion image with signal hyperintensity in stroke region. The bottom row shows the ASL perfusion image with hyperperfusion signal from the region that surrounded the stroke region. The presence of hyperperfusion following acute stroke is a good prognostic feature, since it indicates a reversible brain tissue region (Zaharchuk et al 2012a).

noise or motion artifacts, which is proportional to unsubtracted signals, are therefore reduced. Another technique, pseudocontinuous labeling, is demonstrated to maximize the labeled signal by continuously inverting blood spin that passes through the labeling plane (Dai et al 2008). Due to the substantial development described above, a consensus paper has recently been published (Alsop et al 2015). The current recommendation is to used long pseudocontinuous labeling (1800 ms) and long post labeling delay (1800 ms), followed by a 3D acquisition after background suppression. When applied in practice, however, the current recommended ASL protocol still suffers from several issues, such as cardiac pulsation influence, and leaves rooms for further improvement.

Meanwhile, with the standardization of acquisition protocols through the ASL white paper and implementation of ASL from the vendors, ASL technique has been widely available throughout clinical and research settings. As a consequence, the ASL data processing follows as a high-demanding field. Nonetheless, the non-trivial processing procedures which involves complex general kinetic modeling raised the bar for extracting insights from acquired data for the larger community. In response, several ASL toolboxes have been developed to meet such a need. For example, the MATLAB-based ASL toolbox developed by Wang et al. (Wang et al 2008) and Linux-based BASIL package developed by Chapell et al. (Chappell et al 2009) provide essential function modules from CBF quantification to group statistical analysis. Not surprisingly, when it comes to downloadable toolboxes in neuroimage analysis, most users may have experienced the frustration of software compatibility issue, including operating system platforms, image analysis software upgrades, depended package installing. These issues may appear daunting to many of the end users, such as radiologists, neurologists, psychiatrists, neuroscientists, who are exactly the crowd we want to advocate this technique to. As such, a fully-automated and frustration-free ASL data processing tool is highly desirable in the clinical and neuroscience community.

1.1.2 Motives, strategies, and challenges in vascular compliance imaging

While perfusion imaging enables assessment of capillary healthiness, vascular compliance imaging provides an important measure of the other side of the spectrum, the large arteries (Glasser et al 1997). Vascular compliance represents the ability of a vessel to dilate or increase volume in response to an increase in blood pressure. This buffering mechanism helps to reserve the pulsatile flow in large arteries and convert them to continuous flow into capillaries, which will protect the

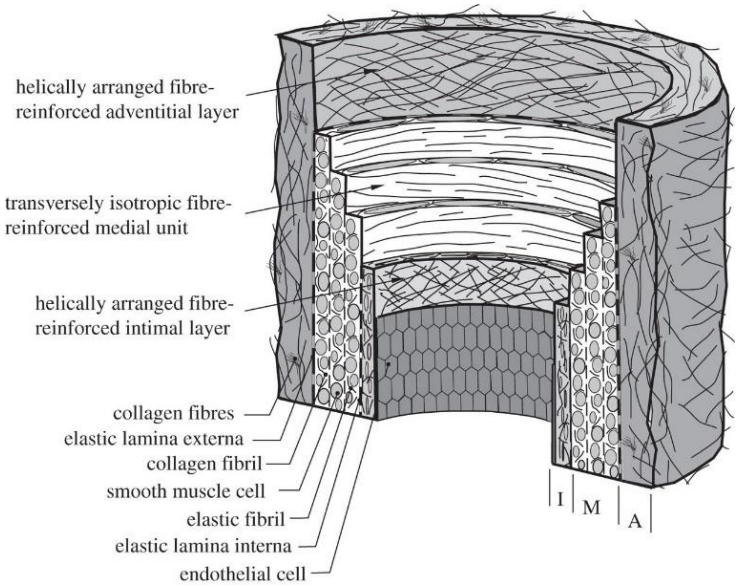

Figure 1.3 Illustration of microstructures of artery vessel wall.

Arteries possess a three-layer structure consisting of an inner layer - intima (I), middle layer - media (M), and outer layer - adventitia (A). The intima is composed mainly of a single layer of endothelial cells. The media is composed of smooth muscle cells, a network of elastic and collagen fibrils. The adventitia is the outermost layer surrounded by thick bundles of collagen fibrils arranged in helical structures (Gasser et al 2006).

capillary bed from being disrupted by pulsation. The vascular compliance is predominantly contributed by to scaffolding proteins, namely collagen with strong tensile strength and elastin that provides elasticity to the vessel wall (see Figure 1.3). When compromised, a stiffened artery could potentially cause series of vessel-related complications. For example, a decreased vascular compliance can increase the risk of stroke via several aspects, including an increase in central pulse pressure, influencing arterial remodeling both at the site of the extracranial and intracranial arteries, increasing carotid wall thickness and the development of stenosis and plaques, the likelihood of plaque rupture, and the prevalence of cerebral white matter lesions (Laurent et al 2006). Normal aging represents a major parameter that associated with the loss of elastin and

therefore vascular compliance (Laurent et al 2005, Zieman et al 2005). Apart from dominant effect of age, several pathophysiological conditions, including obesity, hypertension, diabetes, are also associated with increased arterial stiffness (Mullan et al 2002, Orourke 1990, Zebekakis et al 2005).

As a result, vascular compliance is now accepted as the most important determinants of increasing systolic and pulse pressure in aging societies, thus afford a major contribution to cerebrovascular and myocardial disease. Numerous noninvasive imaging techniques have been developed and applied to evaluate vascular compliance or arterial stiffness. Ultrasound echotracking technique represents a standard method in this field (Laurent et al 2006, Pannier et al 2002). In particular, indices of local stiffness of superficial arteries, such as carotid, can be estimated by measuring the diameter and its change during a cardiac cycle from ultrasound data in conjunction with the local pulse pressure. This technique possesses the advantage of straight-forward measuring on focal artery compliance without requiring assumptions of the models of circulation. Various sites along the arterial tree can be easily accessed by ultrasound echotracking, including aorta, common carotid artery, common femoral artery, brachial artery, and radial artery (Cheung et al 2007, Tanaka et al 2000). However, ultrasound eachotraking of cerebral arteries remains difficult because the skull reflects most of the ultrasound waves, making the intracranial arteries a forbidden region for eachotraking technique. To solve the issue, another ultrasound-based technique, transcranial Doppler ultrasound (TCD), becomes available to measure cerebral vascular compliance (Carrera et al 2011b, Kim et al 2009). TCD relies on the detecting the waveform of blood flow velocities changes within cardiac cycle from the accessible cerebral arteries, such as middle cerebral artery, and derives the indices of vascular compliance via a conversion model. Although the availability of TCD enables the possibility of cerebral vascular

compliance assessment, it cannot obtain arterial volume or diameter directly and thus a quantitative compliance measure is difficult.

For the MR-based methods, two ASL-based MRI techniques have been developed to estimate the cerebral blood volume (CBV) change between systole and diastole recently. Yan et al. (Yan et al 2012, Yan et al 2016) demonstrated that by tracking the ASL signal time course with multi-phase bSSFP after pulsed spin labeling, one may quantify arterial CBV (aCBV). Then the aCBV of systole or diastole can obtained when the multi-phase bSSFP ASL is triggered at corresponding cardiac phase. One shortcoming of this technique is that its single-slice acquisition manner limits the spatial coverage on the 3D extended arterial structure. The other ASL-based method, reported by Warnert et al. (Warnert et al 2015b), estimates aCBV similarly by fitting a model of arterial input function to the multi-delay pulsed ASL data. The aCBV of diastole (systole) is thus obtained after binning the ASL data retrospectively to diastolic (systolic) cardiac phase. Previously, vascular space-occupancy (VASO) technique was developed to detect brain stimulation induced CBV change in capillary bed (Lu et al 2003, Lu & van Zijl 2012), which has the potential to be adapted to measure aCBV change of larger arteries between systole and diastole. Therefore, the VASO-based imaging method to be developed may relieve the situation lacking effective cerebral vascular compliance techniques.

1.2 Specific aims

The overall goal of this thesis is to provide potent tools for non-invasive, quantitative imaging of brain perfusion and vascular compliance in both normal physiology and

cerebrovascular disease. As mentioned in previous section, numerous techniques have been developed yet challenges still remains. Consequently, the specific aims of this thesis are to:

1.2.1 Aim 1: Devise an improved ASL technique for brain perfusion measurement.

We will identify and quantify the effect of physiological noise such as cardiac pulsation in the ASL protocol that is recommended by white paper. Accordingly, we will devise an improved pseudo-continuous ASL (PCASL) sequence, termed as cardiac-triggered PCASL, to minimize the noise and enhance the SNR. We will prove the potential benefit of cardiac-triggered PCASL in the context of two acquisition schemes, specifically single-shot gradient-echo-and-spin-echo (GRASE) 3D and multi-shot cylindrically-distributed-spiral 3D sequences. We will further examine whether cardiac-triggered PCASL can improve the detection of CBF changes, using hypercapnia as a physiological challenge.

1.2.2 Aim 2: Build a cloud-based tool for automated ASL data processing.

We will develop and deploy an online analysis tool, termed as ASL-MRICloud, which allows clinicians and scientists to simply upload their ASL data to our website and, after several minutes, download quantitative perfusion maps and region-of-interest results. We aim to develop and implement analysis pipelines of several common forms of ASL, such as pseudo-continuous ASL (PCASL), pulsed ASL (PASL), multi-delay ASL, and also a comprehensive analysis of the data uploaded.

1.2.3 Aim 3: Develop a vascular compliance mapping MRI technique to quantify the stiffness of intracranial arteries.

We will develop a novel time-resolved VASO-based MR technique to assess the arterial CBV change with respect to pulsation and generate a whole brain vascular-compliance labeled intracranial artery tree of human brain. Arterial stiffness is an important health indicator for vascular reserve. Besides the technical development, we will also perform this technique in young and elderly groups, and will examine the utility of vascular compliance in detecting aging effects on arterial stiffness.

1.3 Significance

Cerebrovascular disease is a major health problem worldwide (Lopez et al 2006, Mortality & Causes of Death 2016). In the United States, it is the fifth leading cause of death. In 2014, it is estimated that more than 130,000 Americans dead in a result of cerebrovascular disease, or more than 40 fatalities per 100,000 people. Thus, if new non-invasive and non-contrast MRI techniques could be developed to make an impact in patients suffer from cerebrovascular disease, it will add substantial value to health care.

ASL perfusion MRI permits non-invasive quantification of blood flow (Detre et al 1992, Williams et al 1992), which is an important physiological parameter that related to the cerebrovascular health (Alsop et al 2000, Chalela et al 2000b). Perfusion imaging plays an important role in several diseases that falls in the category of cerebrovascular diseases. For example, ASL perfusion imaging has been shown potentials to diagnose chronic occlusive disease of intracranial vessels, such as atherosclerosis (Gargiulo et al 2013) and Moyamoya disease (Zaharchuk et al 2011). While in acute ischemic stroke, ASL perfusion imaging can depicts perfusion deficits and perfusion/diffusion mismatches (Rohl et al 2001, Schlaug et al 1999),

referred to as penumbra. Therefore, the development of ASL MRI technique is desirable to measure the perfusion reliably. However, the current ASL protocol recommended by the white paper (Alsop et al 2015) is still suffering from cardiac pulsation influence and needs further improvement.

Another important predictor of cerebrovascular disease is vascular compliance (Cheung et al 2007, Yan et al 2016). Vascular compliance represents the ability of a vessel to dilate or increase volume in response to an increase in blood pressure. This ability of vessel can convert the pulsatile flow in arteries to continuous flow into the capillaries, thus protects the vascular bed from disruptive pulsatile flow (Glasser et al 1997). The loss of vascular compliance has been regarded as a potentially important biomarker of a number of diseases, such as cardiovascular and cerebrovascular diseases, hypertension, diabetes, and Alzheimer's disease (Yan et al 2016). However, there still lacks efficient and reliable approaches to assess the vascular compliance.

1.3.1 A novel cardiac-triggered PCASL provides enhanced SNR in perfusion measurement.

The ASL technique has undergone substantial development over the past few years and a consensus paper has recently been published (Alsop et al 2015). The current recommendation is to use pseudocontinuous labeling with 3D acquisition after background suppression. With the recommended long labeling time (1800 ms) and post-labeling delay time (1800 ms), it is generally thought that the effect of cardiac pulsation should be minimal. However, anecdotally, we often observe that there exist large fluctuations in the difference image (i.e. control-label) intensity from one volume to another. These fluctuations are spatially correlated (i.e. the entire image is bright or dark), thus must be due to sources other than random noise. We hypothesize that, if we can identify the source of these fluctuations and account for it in acquisition, there may be a cost-effective

opportunity for enhancing the SNR of ASL. In this aim, we will show that global signal fluctuations in ASL image is largely attributed to cardiac phase differences from one volume to another, and that cardiac-gated PCASL can increase the SNR by 94% at a modest cost of scan time.

1.3.2 Cloud-based ASL online tool provides comprehensive ASL data analysis

Parallel to the acquisition technique described above, the present project will also develop a novel framework of ASL analysis: a cloud-computing-based tool for comprehensive analysis of ASL MRI, termed as ASL-MRICloud (Mori et al 2016). The general concept of ASL-MRICloud, is that the user only needs to upload the raw ASL data onto our server using any web browser and click the submit button. Then, a few minutes later, quantitative perfusion results will be available for download. The user can then download the outcomes and conduct their study-specific interpretation or statistical analysis. The main strengths of this tool are that it does not depend on local computer operating system or version, does not require downloading or installation of any software, places no constraints on the CPU or memory capacity of the user's computer, and that the developer rather than the user will take the responsibility of software upgrade.

1.3.3 A novel time-resolved VASO MRI technique allows the 3D mapping of intracranial vascular compliance.

In addition to perfusion imaging, we also seek new possible biomarkers that could potentially assist diagnosis or treatment of cerebrovascular disease. One of such is vascular compliance (Glasser et al 1997). Vascular compliance represents the ability of a vessel to dilate or increase volume in response to an increase in blood pressure. This buffering mechanism helps to

reserve the pulsatile flow in large arteries and convert them to continuous flow into capillaries, which will protect the capillary bed from disrupted by pulsation. Vascular compliance is traditionally measured with ultrasound (Gamble et al 1994, Lehmann et al 1998), which can only be applied in large vessels outside the skull. ASL-based methods were proposed, but T1-related signal decay limits its application in small vessels (Warnert et al 2015a, Yan et al 2016). Therefore, a feasible MRI technique to assess the vascular compliance, to be proposed in this study, is highly desirable. In this project, we aim to develop a novel MRI technique based on VASO and assess the aCBV change in accordance with cardiac pulsation. This new technique allows the assessment of intracranial vascular compliance in a 3D fashion. These forms the strong scientific premise of the present thesis.

CHAPTER TWO

2 Cardiac Triggered PCASL Provides a Cost-Effective Scheme to Enhance the SNR of ASL

2.1 Introduction

Arterial Spin Labeling (ASL) MRI permits the measurement of perfusion without the use of contrast agents (Detre et al 1992, Williams et al 1992). However, ASL suffers from an intrinsically low signal-to-noise ratio (SNR), because the difference between control and labeled images is <1% of the original tissue signal. Over the past decade, several techniques have been developed to improve the sensitivity of ASL MRI (Alsop & Detre 1996, Alsop et al 2015, Dai et al 2008, Garcia et al 2005, Gunther et al 2005, Jahanian et al 2011, Restom et al 2006, Robson et al 2009, Wu et al 2007a, Ye et al 2000, Ye et al 1997). For example, background suppression (BS) is now routinely applied to reduce the signal intensity of static tissue (Garcia et al 2005, Robson et al 2009, Ye et al 2000). Pseudocontinuous labeling scheme was developed to increase the labeling efficiency of the continuous ASL method (Alsop et al 2015, Dai et al 2008, Wu et al 2007a). However, further enhancing the signal or reducing the noise remains an essential mission of ASL technical development efforts.

Noise in ASL can be attributed to thermal or physiological factors, e.g. cardiac pulsation. With the recommended long post-labeling delay time (1.8 seconds) and background suppression (Alsop et al 2015), it is generally thought that the effect of cardiac pulsation should be minimal (Kazan et al 2010, Verbree & van Osch 2017). However, it is often observed that there exist large fluctuations in the difference image (i.e. control-label) signal intensity from one image volume to another, especially in regions with large blood vessels. These fluctuations are spatially correlated (i.e. the entire image is bright or dark), thus suggesting a physiological origin rather than random noise. We hypothesize that, if one can identify the source of these fluctuations and account for them in acquisition, there may be a cost-effective opportunity for further enhancing the SNR of ASL.

In this work, we first demonstrated that global signal fluctuations in ASL images are largely attributed to cardiac phase differences from one image volume to another. Then we designed a new ASL sequence, referred to as cardiac-triggered PCASL, and showed that this sequence can substantially suppress such fluctuations and thereby increase the SNR, at a modest cost of scan time. We demonstrated the potential benefit of cardiac-triggered PCASL in the context of two acquisition schemes, specifically single-shot gradient-echo-and-spin-echo (GRASE) 3D (Fernandez-Seara et al 2005, Gunther et al 2005) and multi-shot cylindrically-distributed-spiral 3D sequences (Li et al 2016, Turley & Pipe 2013). We further examined whether cardiac-triggered PCASL can improve the detection of CBF changes, using hypercapnia as a physiological challenge (Aslan et al 2010, Donahue et al 2014, Ho et al 2011, Su et al 2016).

2.2 Methods

2.2.1 General

Experiments were performed on a total of 16 healthy subjects (age 27±5 years, 9 males, 7 females) using a 3 T MRI scanner with a 32-channel receive-only head coil (Philips Healthcare, Best, The Netherlands). Informed consent was obtained using a protocol approved by the institutional review board. We conducted three sub-studies in this work.

2.2.2 Study 1: Proof of principle of cardiac-triggered PCASL in single-shot 3D GRASE acquisition

Eight healthy subjects (3 males) were scanned in this sub-study. A total of ten ASL scans were performed on each participant. Five of them were a regular (non-triggered) PCASL and the other half were a cardiac-triggered PCASL. The repetitions allowed the assessment of coefficient-of-variation (CoV) across runs. For the non-triggered sequence, a pulse oximeter (Invivo, Gainesville, FL) was attached to the index finger of the subject and the timing of cardiac pulse was recorded with reference to the pulse sequence timing (specifically time of the excitation RF pulse). This allows the investigation of the relationship between PCASL signal intensity and cardiac phase. A single-shot 3D GRASE (Fernandez-Seara et al 2008, Gunther et al 2005) acquisition was used in this proof-of-principle study, because cardiac pulsation primarily affects the signal intensity in a single-shot scan whereas its effects in a multi-shot acquisition are more complex.

For cardiac-triggered PCASL (see Figure 2.1 for diagram), the sequence is similar to the non-triggered one except that, after the acquisition module of the previous TR, the scanner will wait for the next cardiac pulse before starting the sequence components of the next TR. The time gap between the cardiac pulse and the beginning of the next TR was 6 ms, which was the shortest

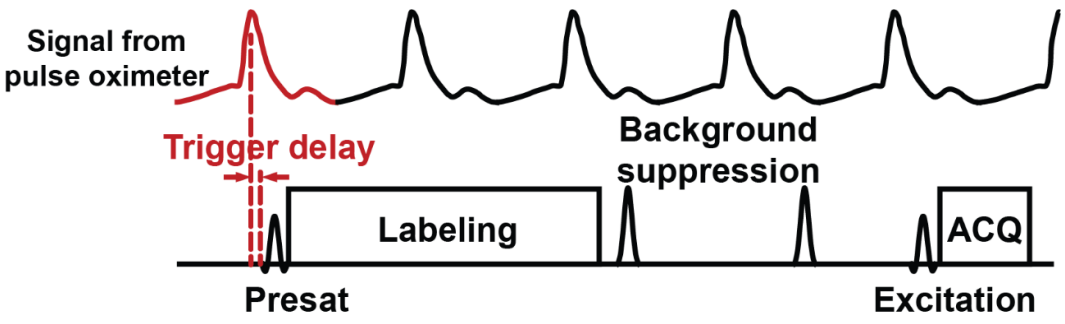

Figure 2.1 Schematic diagram of the cardiac-triggered PCASL pulse sequence. The scanner awaits the next cardiac pulse to begin a TR. The ASL sequence is a PCASL with two background-suppression pulses. The labeling duration and post-labeling delay followed recommendations of the consensus paper.

time allowed on our scanner. This time was necessary for the real-time algorithm to detect the pulse and for the hardware to respond to the trigger. The triggered sequence ensures that the cardiac phase of the beginning of each TR is matched. This scheme does increase the scan duration, ranging from 0 to one full cardiac cycle per TR. On average, the scan duration of the triggered scan was 20.9±4.3% (N=8) longer than non-triggered PCASL. Ten pairs of control/label images were acquired in both regular and cardiac-triggered PCASL. The average scan duration of the non-triggered and triggered PCASL was 1 min 24 sec and 1min 40 sec, respectively.

Other scan parameters followed recommendations of the ASL consensus paper (Alsop et al 2015). We used PCASL labeling with background suppression. Imaging parameters for the PCASL sequence were: labeling duration = 1800 ms, post labeling delay = 1800 ms, FOV = 180×180×104 mm^3, 13 slices, voxel size = 4.5×4.5×8 mm^3, SENSE factor on phase encoding direction = 2.2. The background suppression module contains a pre-saturation pulse placed 10 ms before the labeling module and two adiabatic inversion pulses placed 80 ms and 1300 ms after end of labeling, respectively.

To further confirm that the signal fluctuations observed in the PCASL data are attributed to cardiac pulsation, a cardiac-gated time-resolved phase contrast (PC) MRI was performed to measure the blood flow velocity in the middle-cerebral-artery (MCA) as a function of cardiac phase. The following parameters were used: FOV = 200×200 mm^2, matrix = 400×400, FA = 15°, TE = 9.2 ms, VENC = 100 cm/s, 15 phases with an interval of 60 ms, a single coronal slice of 5-mm thickness at right MCA was imaged with a scan time of 6 min.

Data analysis was conducted using the software SPM (University College London, UK) and in-house MATLAB (MathWorks, Natick, MA) scripts. Image subtractions were performed between the control and labeled images. CBF values in ml/100g/min were calculated from the difference images using a general kinetic model (Alsop et al 2015). Cardiac phase at which the excitation RF pulse was played out was determined based on its location within the R-R interval, and was written in radians (ranging from 0 to 2π) (Wu et al 2009). Relationship between ASL signal and cardiac phase was assessed. CoV was calculated using standard deviation across the five scans divided by their mean. Both voxel-wise map and region-of-interest values were obtained for the CoV. Within each scan, temporal SNR (tSNR) was calculated as mean across dynamics divided by their standard deviation.

To compare the cardiac-triggered results with other ASL physiological-correction methods, in two additional analyses, we used the regular pCASL data but performed CompCor (Component based noise correction method) (Behzadi et al 2007) and RETROICOR (Image-based method for retrospective correction) (Glover et al 2000, Restom et al 2006) approach, respectively, to factor out physiological fluctuations in the ASL data. In the CompCor analysis, signals in voxels with the highest standard deviations were used to extract physiological fluctuations and then employed as regressors to correct the ASL data (Behzadi et al 2007). The residual signal after regression was

used for control/label subtraction and averaging. In the RETROICOR analysis, the measured signal was fitted to 4 Fourier functions of cardiac phase obtained from the pulse oximeter and the residual signal was used for further subtraction and averaging. CoV was compared among these methods.

2.2.3 Study 2: Cardiac-triggered PCASL in segmented 3D PCASL

Since segmented 3D PCASL is a more widely used acquisition scheme due to its higher spatial resolution and larger spatial coverage, we next applied a segmented 3D cylindrically-distributed-spiral TSE acquisition (Li et al 2016) and compared cardiac-triggered PCASL with conventional PCASL. Five subjects were studied. The parameters used in this study were identical to those in Study 1 except for the following: FOV = 200×200×120 mm^3, voxel size = 3×3×4 mm^3, 22 segments, echo train length (ETL) = 9, no parallel imaging acceleration, one pair of control and labeled images. For the acquisition of one segment, a centric view ordering was used in the slice encoding direction, which placed the first echo of the echo train at the center of k_z-space and later echoes alternatively toward the two edges. A total number of 198 spiral interleaves was acquired to cover the whole k-space. The 198 spiral interleaves were evenly spaced along the k_z encoding direction, and any adjacent interleaves were rotated by the golden angle in the k_x-k_y plane (Li et al 2016). Scan duration was around 3 min 45 sec for triggered and 3 min 8 sec for non-triggered sequence. Both sequences were repeated 4 times and a voxel-by-voxel CoV map was calculated. The raw MRI k-space data of 3D spiral PCASL was reconstructed offline using the Graphical Programming Interface software (http://gpilab.com) (Zwart & Pipe 2015).

2.2.4 Study 3: Sensitivity to perfusion changes

To further examine whether cardiac-triggered PCASL can enhance the sensitivity of ASL in detecting perfusion changes, in three subjects we studied CBF differences between normocapnia (NC) and hypercapnia (HC). The subject inhaled room air for 3 min, followed by HC challenge (5% CO_2, 21% O_2, and 74% N_2) for 5 min (Aslan et al 2010, Xu et al 2011). Data in the first 2 min of the HC period was discarded to allow the subject to reach a new steady state of end-tidal CO_2 ($EtCO_2$) level. ASL signals of the room air period and the last 3 min of the HC period were used to evaluate hypercapnia-induced CBF change. For comparison, regular PCASL was also performed using the same paradigm. The acquisition parameters are the same as those of Study 1 except that the number of averages was 20 for regular PCASL and 17 for triggered PCASL, so that both can be completed within 3 min. Voxel-wise paired t-test was performed between HC and NC ASL images to determine whether there were any voxel-level statistically significant differences ($P < 0.05$). Voxel-wise t-score on CBF difference images between NC and HC conditions was also calculated using mean value across averages divided by their standard error.

2.3 Results

2.3.1 Study 1: Proof of principle of cardiac-triggered PCASL in single-shot 3D GRASE acquisition

Figure 2.2a top row shows 10 volumes of CBF maps using the regular PCASL. Their whole-slice-averaged values are displayed as blue lines. It is apparent that the measured CBF images exhibit pronounced fluctuations across image volumes.

The source of such fluctuations is illustrated in Figure 2.2b, which plots the control (blue circles) and labeled (blue triangles) signals as a function of the cardiac phase at the time of

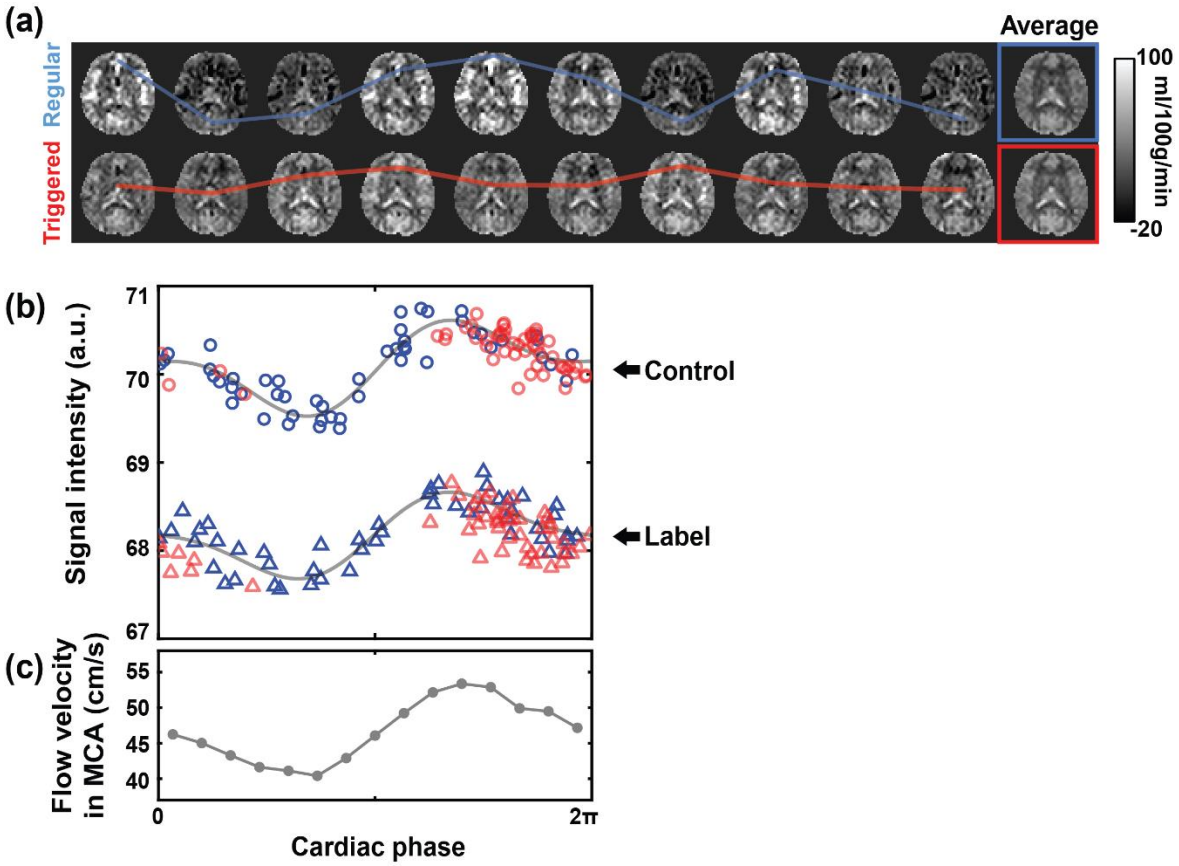

Figure 2.2 Cardiac pulsation effects in a single-shot 3D PCASL.

(a) Ten consecutive measurements of CBF images and their corresponding averages (colored box on the far right) from a representative subject. The top (bottom) panel shows the regular (cardiac-triggered) PCASL. The blue and red curves indicate whole-slice averaged signal intensities, illustrating a greater signal variation in the regular sequence. (b) ASL control and label signal intensities of 50 measurements as a function of cardiac phase. Data acquired with regular (cardiac-triggered) PCASL are shown in blue (red) symbols. Control (labeled) signals are shown in circles (triangles). The gray curves represent the data fitting to 2nd-order Fourier series. (c) Flow velocity in a middle-cerebral-artery (MCA) as a function of cardiac phase, illustrating that the signal fluctuation patterns in ASL are the same as the flow pattern in major arteries.

excitation. For completeness, data points from all five repeated scans are displayed (for a total of 50 image volumes). It is apparent that both control and labeled signals are modulated by the cardiac phase. Interestingly, the control and labeled curves have a similar (instead of upside-down) shape (see Discussion section for more explanations). The vascular origin of the fluctuations is further confirmed by the temporal pattern of the blood flow in the middle-cerebral-artery (MCA) (Figure 2.2c).

Volume-by-volume CBF images of the cardiac-triggered PCASL sequence are shown in Figure 2.2a bottom row. It can be seen that the image intensity and averaged CBF value (red line, Figure 2.2a) are less variable compared to the regular sequence. Figure 2.2b shows the cardiac-triggered PCASL signal (red symbols) as a function of cardiac phase. It can be seen that all image volumes (including both control and labeled images) are of a similar cardiac phase. When calculating the absolute phase differences between the control and labeled images, the cardiac-triggered sequence yielded $0.10\pi \pm 0.04\pi$ radians, which was significantly ($P < 0.003$) lower than that of the regular PCASL ($0.34\pi \pm 0.13\pi$ radians). The remaining phase differences in the triggered scan are likely due to slight variations in duration of cardiac cycle (i.e. heart rate) from one heartbeat to next. Whole-brain CBF obtained from the regular and cardiac-triggered ASL was 33.16±6.34 ml/100g/min and 34.67±5.83 ml/100g/min, respectively, showing no differences ($P = 0.13$) between the techniques.

To visualize the spatial distribution of the fluctuations, CoV maps of both regular and triggered PCASL averaged over eight subjects, as well as their subtractions, are displayed in Figure 2.3a. In the regular PCASL data, large signal fluctuations are apparent in regions with large arterial vessels such as the circle of Willis as well as distally involving the anterior, middle, and posterior cerebral arteries. The cardiac-triggered scheme effectively lowered these fluctuations. The

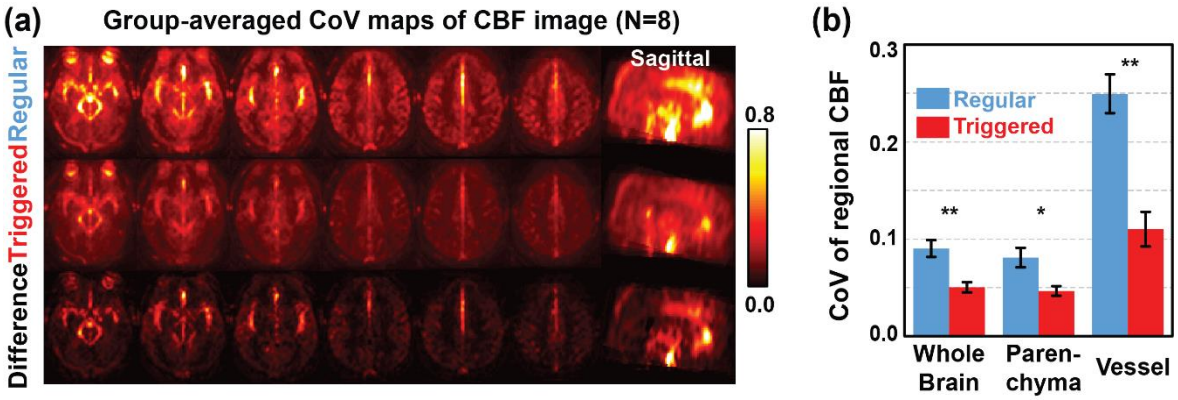

Figure 2.3 Comparison of coefficient-of-variation (CoV) between regular and cardiac-triggered PCASL.

(a) Group-averaged CoV maps (N=8) of CBF images in regular, triggered PCASL, and their difference, respectively. Six representative axial slices and one sagittal slice are shown. (b) Region-of-interest CoV of CBF values in vessel, parenchyma, and whole brain. The error bars indicate standard error (N=8). (* P<0.05, ** P<0.001)

difference of CoV maps revealed that cardiac-triggered PCASL can reduce ASL signal variation in large vessel areas as well as in parenchyma. Comparison of CoV in regions-of-interest (ROI) is shown in Figure 2.3b. In ROIs corresponding to large vessel, parenchyma, and whole-brain, the per-scan SNR (1/CoV) of the cardiac-triggered PCASL data increased by 145±29%, 84±22%, and 94±18%, respectively. Within-scan tSNR is displayed in Figure 2.4, revealing a similar benefit of cardiac triggering.

Additional analyses using the post-hoc correction methods revealed that CompCor and RETROICOR increased SNR of the regular PCASL data by 4.5±9.5% and 19.0±16.4%, respectively, in the whole-brain. But the extent of benefit was lower than that of the cardiac-triggered method. CoV of these post-hoc methods are displayed in Figure 2.5.

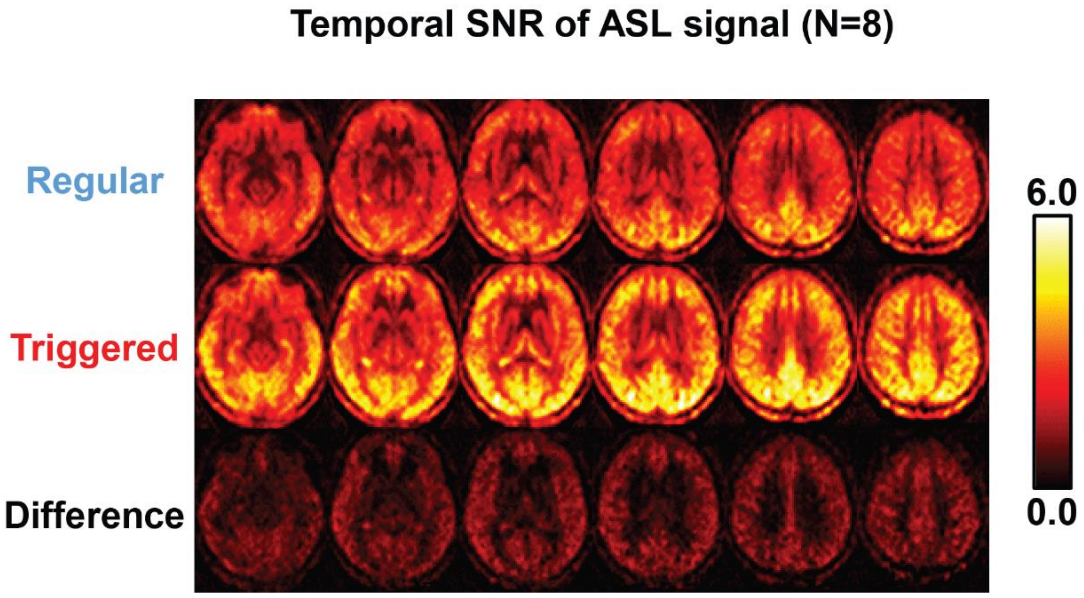

Figure 2.4 Comparison of temporal SNR between regular and cardiac-triggered PCASL.

The whole-brain difference map of temporal SNR, especially in gray matter, reveals the benefits of cardiac-triggered PCASL.

2.3.2 Study 2: Cardiac-triggered PCASL in segmented 3D PCASL

Figure 2.6a shows a comparison between regular and triggered 3D segmented PCASL images. With regular PCASL, the CBF images are contaminated by ring-shaped artifacts (e.g. yellow arrows). In the triggered data, this artifact was not present. Figure 2.6b shows CoV maps using the two methods. It can be seen that, in the regular, segmented PCASL data, high CoV voxels are observed in a considerable portion of the brain including both vessels and parenchyma. This is different from the single-shot PCASL (c.f. Figure 2.3a) where high CoV is only seen in large-vessel regions. This is because segmented acquisition causes the signal fluctuation to spill over along the segmentation direction, resulting in more voxels affected by the artifact. Averaged across

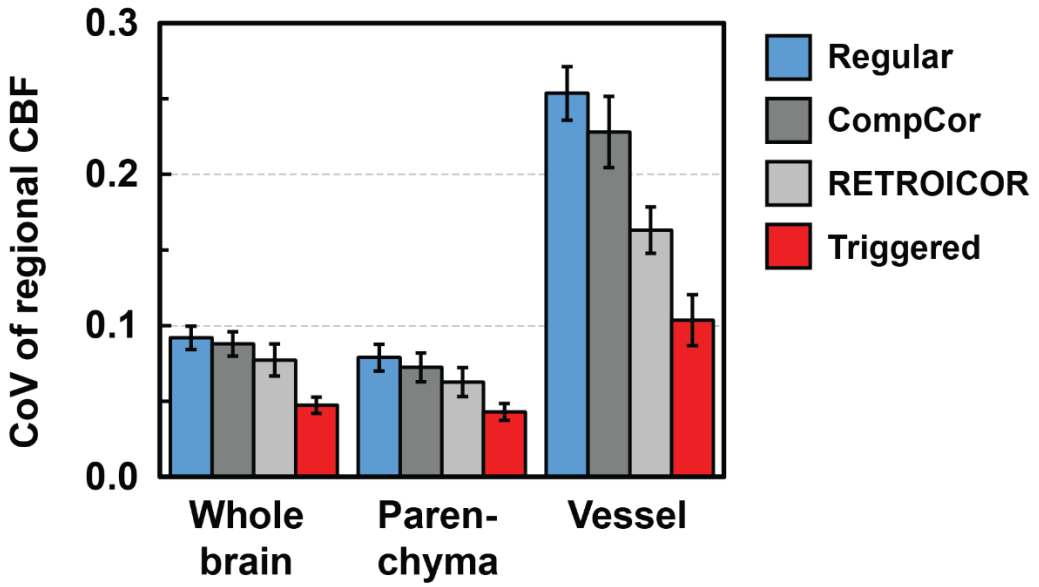

Figure 2.5 Comparison of regional CoV between regular PCASL, CompCor-corrected PCASL, RETROICOR-corrected PCASL, and cardiac-triggered PCASL.
Regions investigated included vessel, parenchyma, and whole brain. The error bars indicate standard error (N=8).

the whole brain, CoV of the triggered ASL image decreased significantly (P<0.01) by 22±3% when compared to regular PCASL (see Figure 2.6c), which corresponds to a 28±4% increase in SNR.

2.3.3 Study 3: Sensitivity to perfusion changes

Figure 2.7 summarizes the CBF images under NC and HC conditions, as well as their difference, for both regular and triggered schemes. The average CBF increase measured by triggered PCASL was 36.7±6.6%, which is similar to the one measured by regular PCASL of 35.8±7.1%. The CBF difference image using the triggered sequence is more stable than the regular

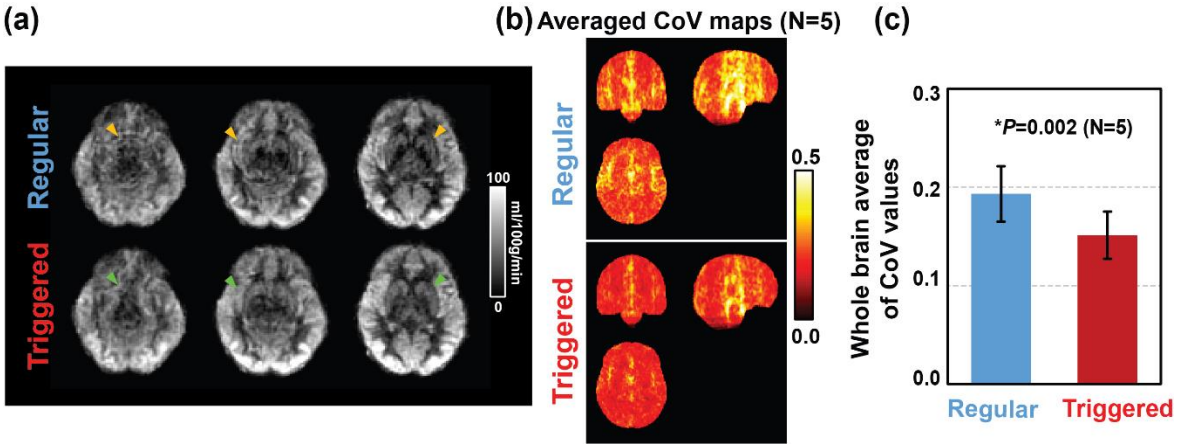

Figure 2.6 Comparison between regular and cardiac-triggered PCASL when using multi-shot 3D spiral acquisition.

(a) Representative slices of CBF maps from a subject. Yellow arrows point to ring-shaped artifacts in the regular PCASL. Green arrows point to the same regions in the cardiac-triggered data, illustrating an absence of artifacts. (b) Group-averaged CoV maps (N=5) of CBF images in regular and cardiac-triggered PCASL. Note that the cardiac fluctuations are smeared along the craniocaudal direction due to segmented acquisition. (c) Comparison of whole-brain averaged CoV values between the two methods. The error bars indicate standard error (N=5).

sequence with fewer bright or dark vascular artifacts. CoV of the difference images was 63±12% smaller in the triggered data. The higher sensitivity of triggered PCASL in detecting perfusion change can be further appreciated by examining the voxel-by-voxel paired t-test results, where triggered PCASL uncovered more activated voxels (right column, Figure 2.7a) ($P < 0.05$) than regular PCASL and revealed overall higher t-scores in histograms (see Figure 2.7b).

2.4 Discussion

In this study, we characterized the effect of cardiac pulsation on ASL signal when using a PCASL protocol recommended by the consensus paper (Alsop et al 2015). We showed that, in single-shot acquisitions, this results in signal instability in regions near large vessels and, in segmented acquisitions, it results in ghosting artifacts and the signal fluctuation is smeared along the segmentation direction to affect more brain regions. To overcome this effect, we developed a cardiac-triggered PCASL scheme that was shown to enhance the temporal SNR by 94% and 28% in single-shot and segmented 3D acquisition, respectively. We further evaluated the sensitivity of cardiac-triggered PCASL in detecting CBF change by using hypercapnia challenge as a model. The results revealed less signal variance and greater statistical power compared with regular PCASL.

2.4.1 Technical considerations

Based on the comparison of CoV (e.g. Figure 2.3b) between the triggered and regular sequence, we estimate that at least 44% of the noise in the ASL data is attributed to cardiac pulsation. The actual fraction could be even bigger because the triggered data may still contain some residual cardiac effects (due to variations in heart rate during the scan). Spatially, the cardiac pulsation effects are most pronounced in regions near large arteries, such as in the base of the brain, around the brain stem, and adjacent to the Sylvian fissure. With multi-shot acquisition, however, the territory of artifacts could further expand along the segmentation direction to cover more brain areas (e.g. Figure 2.6b). Therefore, a scheme to minimize the cardiac pulsation effects in ASL would provide a sizable benefit in enhancing the quality of the ASL data.

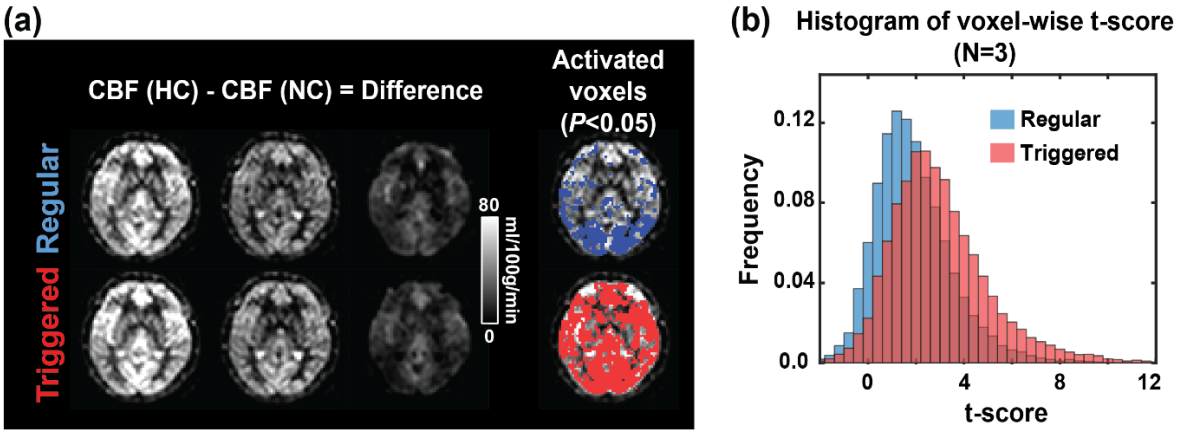

Figure 2.7 Comparison between regular and cardiac-triggered PCASL in detecting perfusion change during hypercapnia challenge.

(a) CBF maps of one subject with normocapnia (NC), hypercapnia (HC), and their corresponding difference map. Voxels showing statistically significant difference ($P < 0.05$) between NC and HC, referred to as "activated voxels", are also displayed (in color). (b) Histogram of voxel-wise t-score associated with CBF difference between NC and HC conditions.

The cardiac-triggered scheme proposed in this work requires a pulse device, which is a standard accessory available on most MRI scanners and is used routinely in cardiac and body MRI, although not usually in neuro scans. The scan time for the cardiac-triggered sequence is slightly longer than the regular PCASL sequence because the sequence needs to wait for the start of the next pulse to begin the next TR. This additional delay is between 0 and 1 cardiac cycle. In our data, the average scan duration of the cardiac-triggered sequence is about 20% longer than the regular PCASL. Considering an SNR increase of 28-94%, this is cost-effective and is considerably more efficient than increasing SNR by more averages. It should also be pointed out that, since the cardiac pulsation artifact is particularly severe in regions near vessels, this technique may be crucial in studies of brain perfusion or neural abnormality in selective brain regions such as

hippocampus (Alsop et al 2008, Rusinek et al 2011) or insula (Chen et al 2011b, Fernandez-Seara et al 2011), which happen to be located next to major vessels.

The trigger point of our sequence was set to be immediately before the pre-saturation pulse. This is because the pre-saturation pulse can "reset" the magnetization of the spins so that the variations in actual TR from one repetition to next will not affect the measured signal intensity and the static signals in the control and labeled images can still cancel out. We had also considered placing the trigger point at the excitation RF pulse. However, in that case, the magnetization recovery time of static spins will be different across TRs, resulting in imperfect cancelation of static signals (Greer et al 2016).

This study also compared the SNR benefit of cardiac-triggered PCASL to those based on post-hoc correction methods. The CompCor correction-based approach has the advantage that it does not require any additional physiological recording, and can provide a modest increase in SNR (see Figure 2.5). The RETROICOR method requires a pulse oximeter to measure the cardiac phase of the data acquisition and has a greater SNR benefit than CompCor. On the other hand, the pulse sequence based approach proposed in this study appears to provide the largest augment in signal stability compared to the post-hoc correction methods. Moreover, it should be pointed out that the post-hoc methods noted above have primarily been used in single-shot ASL MRI. In contrast, the cardiac-triggered method can also be applied in multi-shot acquisitions, which represent a more widely used ASL acquisition scheme in recent literature (Alsop et al 2015).

2.4.2 Physiological considerations

Cardiac pulsation effect in ASL has been a topic of interest in a number of previous studies (Fushimi et al 2013, Restom et al 2006, Verbree & van Osch 2017, Wu et al 2009, Wu et al 2007b).

Wu et al. and Fushimi et al. studied the effect of labeling timing in pulsed ASL (PASL) (Fushimi et al 2013, Wu et al 2007b). A significantly higher CBF was observed when the bolus was labeled at systolic compared with diastolic phases. This CBF disparity was attributed to a difference in the transit delay of labeled spins.

In CASL or PCASL sequences, however, this effect is expected to be smaller because of the long labeling duration used in CASL and PCASL and that the distribution of transit delays is likely similar across TRs. Verbree and van Osch varied the cardiac phase at the end of the labeling period and concluded that the ASL signal is not significantly affected by the end-of-labeling phase despite the expectation that more labeling effect should be observed when the labeling period ends at systolic phase (due to less labeling decay) (Verbree & van Osch 2017). Indeed, our data support the notion that the labeled spins (or its variation across TR) are not the source of the fluctuation seen in our study. Had the number of labeled spins been the reason for the signal fluctuation, we would have seen that the phase-dependence of the control signal would be opposite from the labeled signal. As shown in Figure 2.2b, however, the labeled and control signals actually have the same pattern of cardiac phase dependence. We therefore propose that one possible contribution to the observed fluctuation is that, during the systolic phase, the arterial vessel is extended and more fresh, uninverted spins have arrived at the imaging voxel during the post-labeling delay. Another possible contribution is that faster flow during the systolic phase may also allow a larger number of fresh spins to reach the imaging voxel, independent of the blood volume effect. Regardless the volume or flow pulsation effects, these uninverted spins are present in both control and labeled scans, suggesting that they represent inflowing spins following the label/control bolus. These spins have a different level of magnetization from the static spins which are background suppressed, and thus can cause a signal fluctuation.

2.4.3 Limitations

One limitation of the proposed technique is that it may not be effective in participants whose R-R interval, i.e. heart rate, shows a large variation, because the cardiac triggering is applied at the beginning of the labeling period but not at the time of the excitation RF pulse. Thus, the cardiac phase at the excitation may be out of synchronization in such patients. Another limitation is that the placement of the pulse device on the patient nonetheless represents an additional step in the workflow of the MRI technologist and could be viewed as a burden. Also, the patient will have to use the other hand to move or scratch since movement of the hand that is attached to the placed pulse oximeter may interfere with accurate assessment of cardiac rate/pulse. Similarly, if the pulse oximeter falls off or loses signal due to hand movement, the scan may stall. In order to continue the scan, the operator would need to enter scanner room and adjust the pulse oximeter.

2.5 Summary

We showed that regular PCASL sequence results in ASL signals that are sensitive to cardiac pulsation effects, reducing the fidelity of the data. Cardiac-triggered PCASL can enhance the SNR by 94% and 28% in single-shot and segmented acquisitions, respectively, at a modest cost of scan time. Thus, this technique may represent a cost-effective approach to improve the reliability of ASL. We have demonstrated that the proposed sequence can improve ASL data quality in multiple settings.

CHAPTER THREE

3 ASL-MRICloud Serves as an Online Tool for the Processing of ASL MRI Data

3.1 Introduction

Arterial spin labeling (ASL) MRI is a noninvasive method to quantify cerebral blood flow (CBF). This technique is increasingly used in studies of brain function, physiology, and neurological and psychiatric diseases. All major MRI manufacturers now provide ASL MRI as part of their product sequence. Major multi-site studies such as Alzheimer's Disease Neuroimaging Initiative (ADNI) (Jack et al 2008), ABCD (Zaharchuk et al 2012b), and UK Biobank study (Miller et al 2016) have also included ASL MRI in their scan protocol.

As acquisition of ASL perfusion data becomes more accessible to the broader imaging community, processing of ASL data emerges as a timely issue. ASL is a specialized pulse sequence and its signal is determined by a kinetic model that describes the time-dependence of arterial spins as they travel to capillary and tissue. Many potential users of ASL such as radiologists, neurologists, psychiatrists, and neuroscientists may not have the expertise to carry out these

sophisticated modeling procedures. Therefore, a turnkey solution for ASL data processing is expected to significantly facilitate the wide application of this promising technique.

In this work, we developed a cloud-based tool for ASL data processing, termed as ASL-MRICloud. This tool is based on the infrastructure of MRICloud.org (braingps.mricloud.org) (Li et al 2017b, Liu et al 2016, Mori et al 2016). Compared with other existing ASL toolboxes (Abad et al 2016, Chappell et al 2009, Hernandez-Garcia et al 2010, Liang et al 2015, Shirzadi et al 2015, Wang et al 2008), which are based on local computing, ASL-MRICloud is based on cloud computing. This user only needs to have a web browser for uploading data and downloading results, and the processing is fully automatic. The main strengths of this tool are that it does not depend on local computer operating system, does not require installation of any software, places no constraints on the CPU or memory capacity of the local computer, and that the developer rather than the user will take the responsibility of software upgrade.

The ASL-MRICloud tool was implemented to be compatible with data acquired by scanners from all major MRI manufacturers. Given the presence of multiple ASL variants, our tool was made to be capable of processing several common forms of ASL scheme, including pseudo-continuous ASL (PCASL), pulsed ASL (PASL), and multi-delay ASL. The ASL-MRICloud tool is also compatible with background suppression schemes as well as multi-slice and 3D acquisitions, which require slightly different equations in perfusion quantification. A quality control index is also provided by the tool. Furthermore, an important advantage of our tool is that the processing of ASL data is integrated with a sophisticated T1-based multi-atlas brain segmentation tool in the MRICloud platform. Consequently, the outcome CBF results are presented in Montreal-Neurologic-Institute (MNI) template space with regional values of up to 289 standard brain structures, which can readily undergo statistical analysis. This article provides

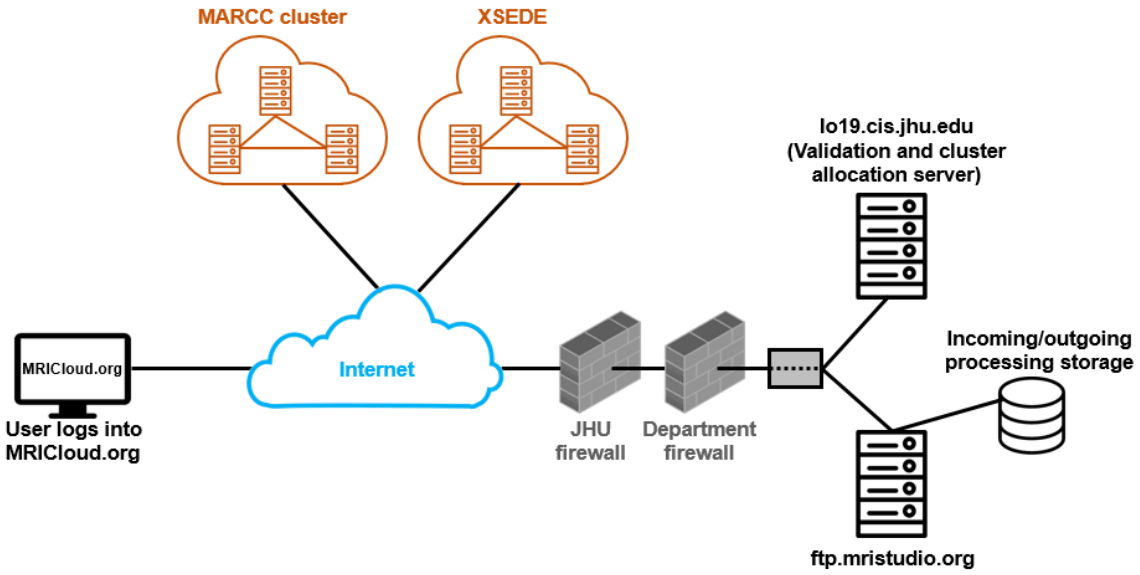

Figure 3.1 Illustration of the MRICloud server components.

After the user login the MRICloud.org and submit the processing job, MRICloud.org generates a .zip from the users' data and sends it to the anonymous FTP server (ftp.mristudio.org) behind the JHU firewall. Another server (io19.cis.jhu.edu) monitors the incoming queue for newly uploaded jobs. Upon arrival, this server validates the data, identifies a computation resource, and copies the data to one of the clusters (MARCC cluster and XSEDE). The data are then queued using an SSH signal. The FTP server (ftp.mristudio.org) also monitors job completion and updates the job status at MRICloud.org (Mori et al 2016).

a description of the ASL-MRICloud tool in terms of its functionalities, main algorithms used in the pipeline, typical steps to use it, and representative results.

3.2 Methods

3.2.1 General concept of ASL-MRICloud

The framework of the ASL-MRICloud is illustrated in Figure 3.1. The proposed ASL-MRICloud with an option of the T1 multi-atlas brain segmentation is highly computing intensive. Instead of performing computational analysis of the ASL data on the user's local computer, the tool places the computational and programming burden on our internal or publicly available computation resources such as Computational Anatomy Gateway via XSEDE (www.xsede.org) and MARCC clusters (see orange diagrams in Figure 3.1). To start, the user only needs to upload the ASL data onto the server using a web browser and click the submit button. Then, a few minutes later, quantitative perfusion outcomes will be available for download. The user can then download the outcomes and conduct their study-specific statistical analysis. As for the software upgrade and maintenance, the developers will take the responsibility and free the user from installing updates or patches.

3.2.2 Major steps of using ASL-MRICloud

When the user browses the ASL-MRICloud website, https://braingps.mricloud.org/ asl.v2, a main page, shown in Figure 3.2, is displayed. The user is requested to complete the following steps:

1. Upload the ASL file. At present, the required file format is ANALYZE (.hdr and .img). This is because this file format does not contain Patient Health Information (PHI), thus it is compatible with Health Insurance Portability and Accountability Act (HIPAA) regulations. The user can generate ANALYZE files using their own program or can use a DICOM-to-ANALYZE conversion program that can be downloaded from the ASL-MRICloud website. Our program has been tested for ASL data collected on General Electric, Philips, Siemens, and Toshiba MRI scanners.

2. Upload an optional equilibrium magnetization (M0) file. Information of M0 is necessary for quantitative estimation of CBF in the unit of ml/100g/min. If an M0 image was acquired in the experiment, the user should upload the file in this step. If an M0 image was not acquired, the user can skip this step. The processing algorithm (described below) will use the ASL data to estimate M0.
3. Upload an optional T1 anatomic file. Most research requires the CBF image to be registered to high-resolution anatomic space or standard template, e.g. MNI, space. Therefore, the tool gives the user an option to upload a high-resolution T1 data set for registration and normalization purposes. The T1 data set is not the raw image file. Instead, the user can use a companion tool, T1-MRICloud, to first process the T1 image. Then they can upload the output file of the T1-MRICloud, a .zip file, which contains comprehensive information including individual-space T1 image, MNI-normalized T1 image, brain parcellation results, as well as the transformation matrix.
4. Provide imaging parameters. In a series of pull-down menus and numerical boxes, the user is requested to select or provide sequence information that is necessary for CBF quantification. This includes the type of ASL sequence (e.g. PCASL or PASL), the order of data presentation (control first or label first), image acquisition method (2D or 3D), labeling duration, post-labeling delay, background suppression timings, as well as assumptions necessary in the kinetic model such as blood T1, brain-blood-partition coefficient, and labeling efficiency.

Once these steps are completed, the user can click the “submit” button and the job will be placed in a queue for processing. The typical waiting time before the results are available for downloading is approximately 5 minutes.

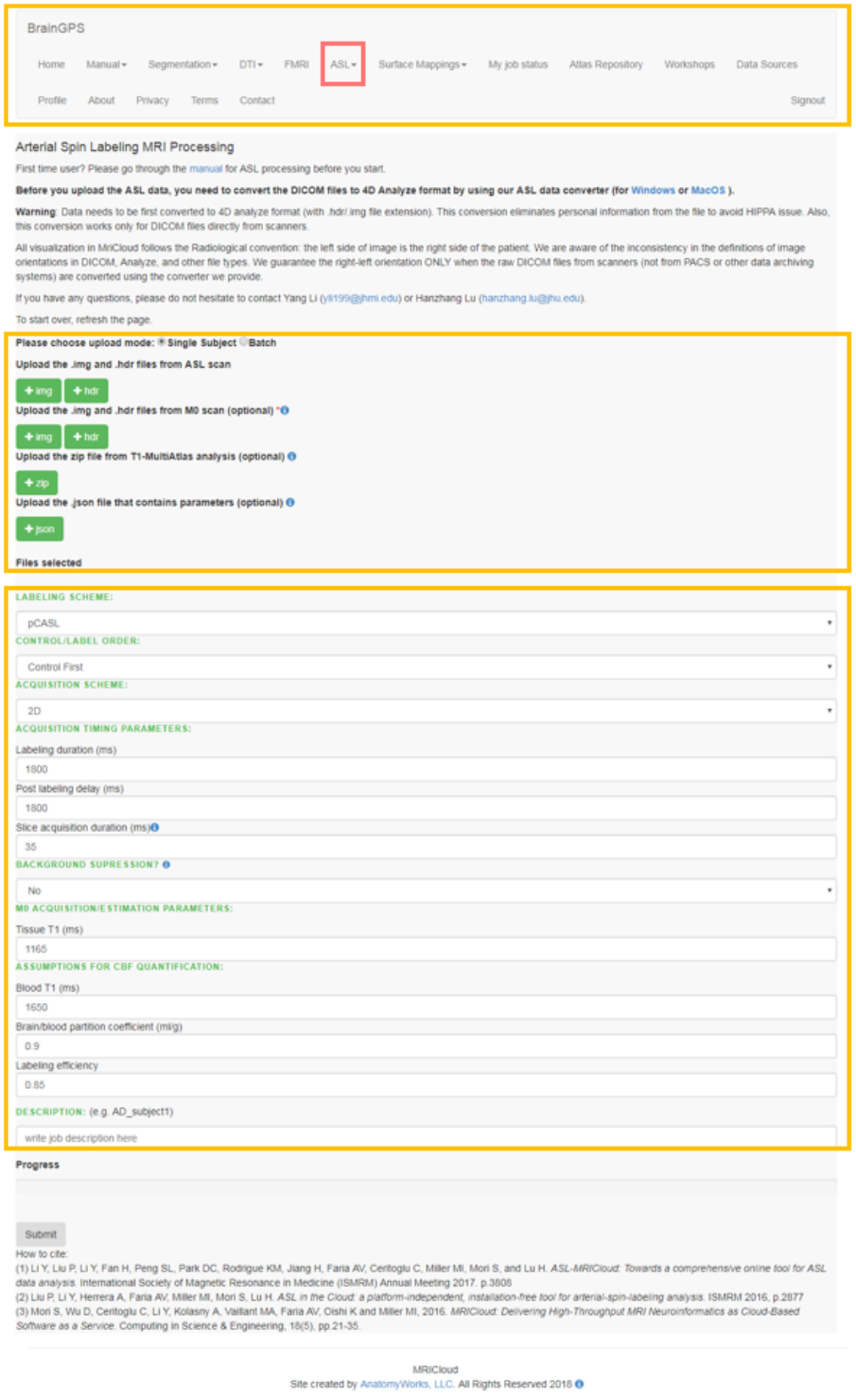

MRICloud toolboxes

ASL dataset uploading

ASL parameters

Figure 3.2 The web interfaces of MRICloud homepage and ASL-MRICloud.
The ASL-MRICloud tool is highlighted by the red box.

3.2.3 Major functionalities of ASL-MRICloud

Quantification of CBF using single-delay ASL

The processing pipeline of single-delay ASL is illustrated in Figure 3.3. The ASL image series were corrected for motion, in which all control and label images were aligned to their respective first time point. The difference images (i.e. control-label) were then calculated. Next, information about M0 was determined. If the user had uploaded an M0 image, a voxel-by-voxel M0 map would be used. Additionally, in cases when the uploaded M0 image was acquired with a TR of less than 5 seconds, the image will be adjusted for T1 recovery before being used as M0 map. If an M0 image is not uploaded, a global M0 will be used in CBF quantification. The pipeline will estimate the equilibrium magnetization from the control images, after accounting all RF pulses present in the pulse sequence and by assuming a tissue T1.

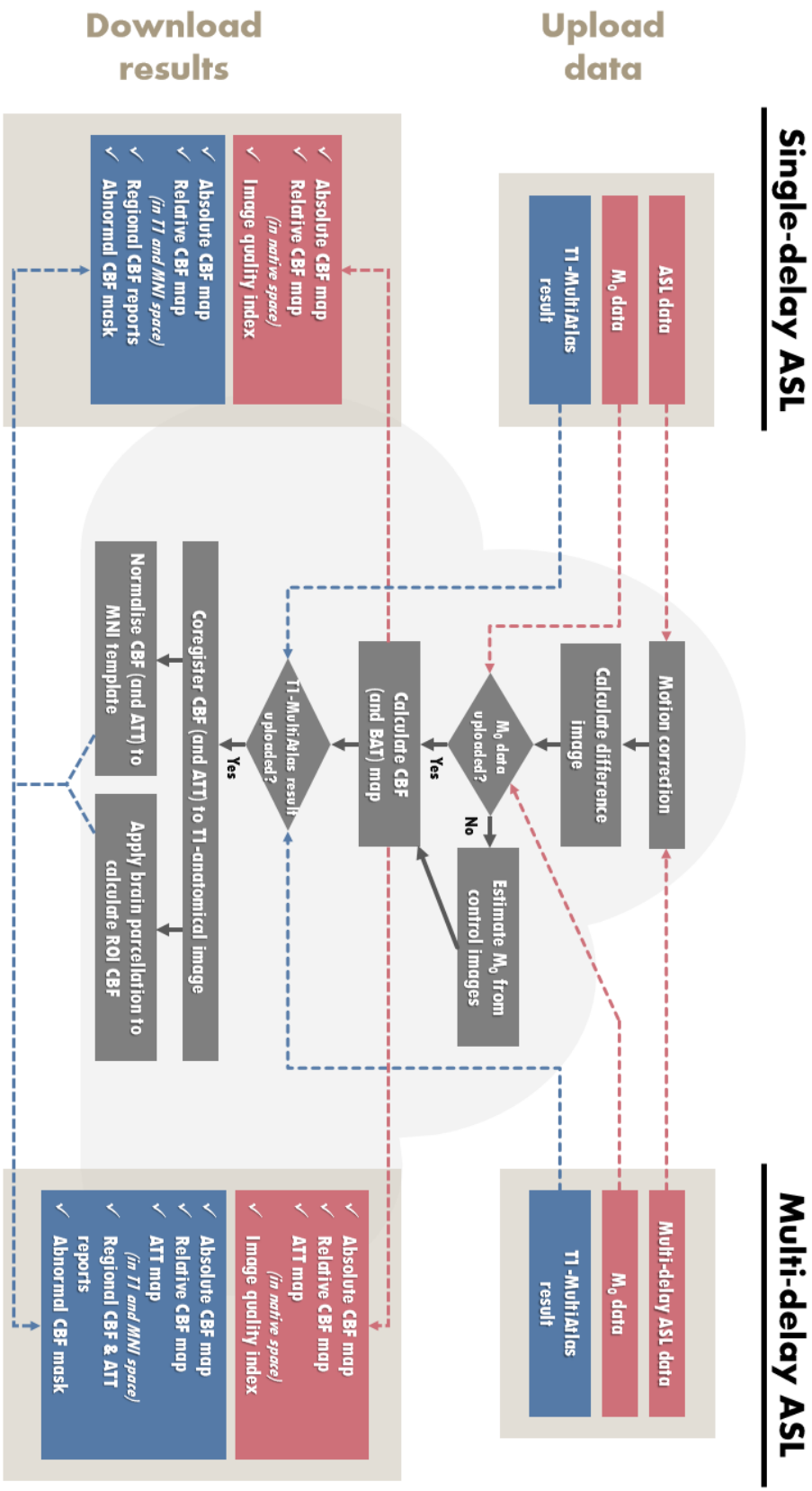
Single-delay ASL
Multi-delay ASL
Upload data
Download results
ASL data
M0 data
T1-MultiAtlas result
Multi-delay ASL data
M0 data
T1-MultiAtlas result
Motion correction
Calculate difference image
M0 data uploaded?
Yes
No
Estimate M0 from control images
Calculate CBF (and BAT) map
T1-MultiAtlas result uploaded?
Yes
Coregister CBF (and ATT) to T1-anatomical image
Normalise CBF (and ATT) to MNI template
Apply brain parcellation to calculate ROI CBF
Absolute CBF map
Relative CBF map
Image quality index
(in native space)
Absolute CBF map
Relative CBF map
(in T1 and MNI space)
Regional CBF reports
Abnormal CBF mask
Absolute CBF map
Relative CBF map
ATT map
Image quality index
(in native space)
Absolute CBF map
Relative CBF map
ATT map
(in T1 and MNI space)
Regional CBF & ATT reports
Abnormal CBF mask

Figure 3.3 Details of ASL analysis procedures on the cloud server.
The pipeline accepts data from both single-delay and multi-delay ASL.

The quantification of CBF follows models described in the ASL white paper (Alsop et al 2015). Specifically, voxel-wise CBF value is obtained by

$$f = \frac{6000 \cdot \lambda \cdot R_{1a}}{2\alpha} \cdot \frac{\Delta M}{M_0} \cdot \frac{e^{PLD \cdot R_{1a}}}{1 - e^{-\tau \cdot R_{1a}}} \quad [1]$$

for PCASL and

$$f = \frac{6000 \cdot \lambda}{2\alpha \cdot \tau} \cdot \frac{\Delta M}{M_0} \cdot e^{PLD \cdot R_{1a}} \quad [2]$$

for PASL. In Eq. 1 and Eq. 2, f is the CBF in mL/100 g/min, λ is the brain/blood partition coefficient in mL/g, ΔM is the difference signal intensity between control and label images, $R_{1a} = 1/T_{1a}$ is the longitudinal relaxation rate of artery blood in Hz, α is the labeling efficiency, and τ is the labeling duration in seconds, and PLD is the post-labeling delay.

The single-delay ASL data can also be processed in a batch mode, in which up to 10 data sets can be uploaded and processed at once.

Quantification of CBF and arterial-travel-time (ATT) using multi-delay ASL

The processing pipeline of multi-delay ASL is illustrated in Figure 3.3. Pre-processing steps of motion correction and control-label subtraction were similar to that of single-delay ASL. For M0 determination, if an M0 image was not uploaded, the pipeline will use the ASL data to estimate a voxel-by-voxel M0 map. In the case of PCASL, the M0 map was obtained by fitting the control signals as a function of PLD to a saturation recovery equation. In the case of multi-delay PASL which is typically acquired using a Look-Locker acquisition scheme, the control signal is fitted to a slightly different equation to account for the Look-Locker acquisition (Li et al 2010, Shin et al 2009),

$$M_{control}(PLD) = M_{ss} \cdot (1 - e^{-R_{1eff} \cdot PLD}) \quad [3]$$

in which $M_{ss} = M_0 \cdot \frac{1-e^{-R_1 \cdot PLD}}{1-cos\,\theta \cdot e^{-R_1 \cdot PLD}}$ and $R_{1eff} = R_1 - \frac{ln(cos\,\theta)}{\Delta PLD}$, θ is the excitation flip angle, and ΔPLD is the interval between excitation pulses.

For quantification of CBF and ATT from the multi-delay ASL data, the signals were fitted to a kinetic model using a nonlinear least-square curve fitting with trust-region-reflective algorithm (Coleman & Li 1996, Thomas & Li 1994). Specifically, for multi-delay PCASL, the signals were fitted to the following equations:

$$\frac{\Delta M(PLD)}{M_0} = \begin{cases} 0, & 0 < PLD + \tau < \tau_a \\ \dfrac{2\alpha \cdot f}{6000 \cdot \lambda \cdot R_{1app}} \cdot e^{-R_{1a} \cdot \tau_a} \cdot \left(1 - e^{-R_{1app} \cdot (PLD + \tau - \tau_a)}\right), & \tau_a \leq PLD + \tau < \tau + \tau_a \\ \dfrac{2\alpha \cdot f}{6000 \cdot \lambda \cdot R_{1app}} \cdot e^{-R_{1a} \cdot \tau_a} \cdot \left(e^{-R_{1app} \cdot (PLD - \tau_a)} - e^{-R_{1app} \cdot (PLD + \tau - \tau_a)}\right), & PLD + \tau \geq \tau + \tau_a \end{cases} \quad [4]$$

in which $R_{1app} = R_1 + \frac{f}{\lambda}$, where R_1 is the longitudinal relaxation rate of tissue in Hz, and τ_a is the ATT. For multi-delay PASL with look-locker acquisition, the signals are fitted to the following equations:

$$\frac{\Delta M(PLD)}{M_0} = \begin{cases} 0, & PLD < \tau_a \\ \dfrac{2\alpha \cdot f}{6000 \cdot \lambda \cdot \delta R} \cdot \left(e^{\delta R \cdot (PLD - \tau_a)} - 1\right) \cdot e^{-R_{1a} \cdot PLD}, & \tau_a \leq PLD < \tau_d \\ \dfrac{2\alpha \cdot f}{6000 \cdot \lambda \cdot \delta R} \cdot \left(e^{\delta R \cdot (PLD - \tau_a)} - 1\right) \cdot e^{-R_{1a} \cdot \tau_d} \cdot e^{-R_{1app,eff} \cdot (PLD - \tau_d)}, & PLD \geq \tau_d \end{cases} \quad [5]$$

in which $\delta R = R_{1a} - R_{1app,eff}$, $R_{1app,eff} = R_1 + \frac{f}{\lambda} - \frac{\ln(\cos\theta)}{\Delta PLD}$, and τ_d is the duration from labeling pulse to the time when the trailing edge of the label reaches the imaging voxel. A voxel-by-voxel fitting of the signals to these equations then yields maps of CBF, ATT, and τ_d.

Presentation of ASL results in anatomic and template spaces

If a T1 data set has been uploaded, the ASL control image will be coregistered to the individual T1 space using a 12-parameter affine transformation, which is also applied to the

parametric maps, e.g. CBF and ATT. Furthermore, all images will be normalized to the MNI space by applying an elastic transformation determined by the T1-MRICloud tool.

Finally, since the T1 data set also contain parcellation results of the individual brain, regional CBF values up to 289 ROIs will be obtained.

Examination assistance indices

To aid users to conduct further examinations of the CBF maps, we provide two additional indices on each data set. One is an ASL image quality index (QI), which is a categorical scale that indicates the general SNR of the data ranging from 1 (Excellent) to 4 (Poor). To calculate the image QI, voxel-wise standard errors of the ASL difference images were first computed across repetitions. Next, the standard errors were averaged across the whole-brain and divided by whole-brain averaged difference signals, which was then converted to the categorical scale (i.e. 1, 2, 3, or 4) based on predefined thresholds: 0.0 to 0.47 corresponds to 1; 0.47 to 0.73 corresponds to 2; 0.73 to 1.00 corresponds to 3; 1.00 and above corresponds to 4. We further validated the QI by comparing it to the manual ratings of an expert ASL researcher in a large CBF database consisting of 309 healthy volunteers ranging from 20 to 89 years old (Lu et al 2011).

The second index is a voxel-wise mask that indicates potential hyperperfusion and hypoperfusion regions, referred to as perfusion abnormality (Abnorm) index. We first established expected CBF and its normal variation by calculating voxel-by-voxel distributions of relative CBF in our database of 309 healthy volunteers and obtained voxel-wise maps of mean and standard deviation. For a new CBF map that the user uploads, we can then calculate a map of Z-scores based on the mean and standard deviation of the healthy subjects. A p-threshold of 0.005 was used

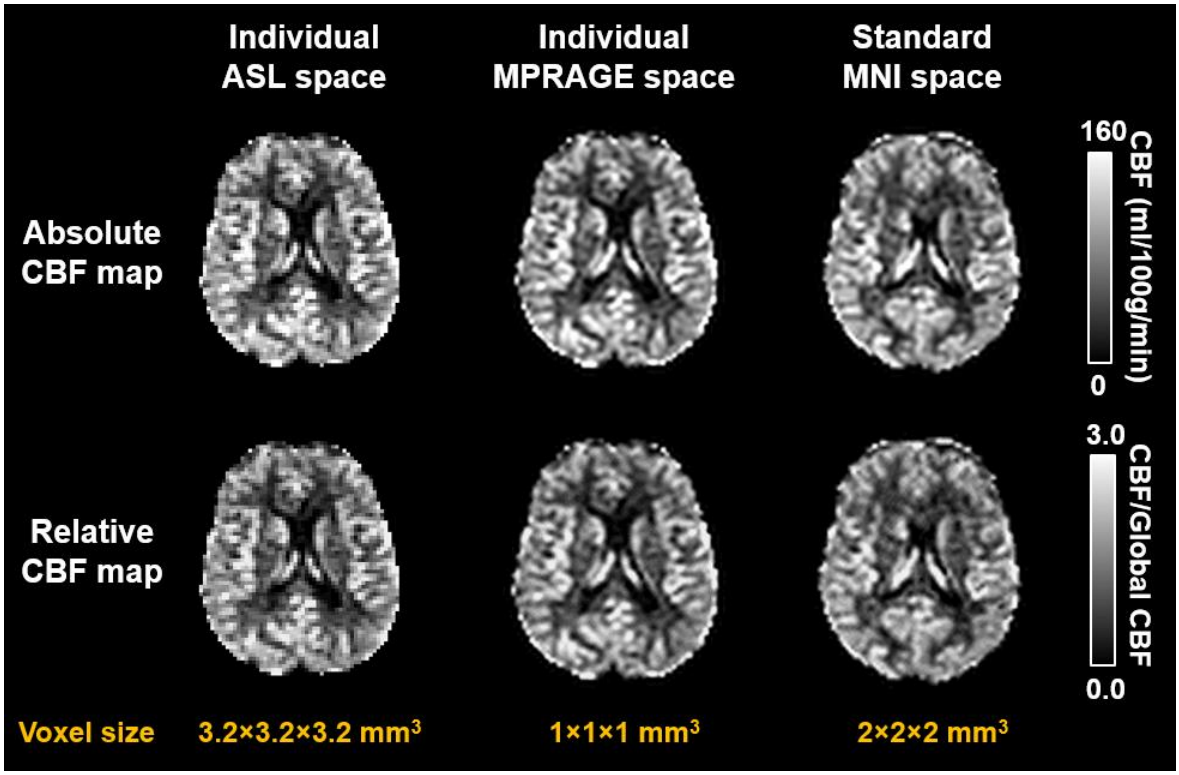

Figure 3.4 CBF maps in multiple spaces generated by the ASL-MRICloud from the dataset of one representative healthy volunteer.

The resolution of each space is listed below the CBF images.

to delineate voxels with abnormal CBF. The Abnorm index was tested on ASL data from Moyamoya patients with arterial stenosis.

3.3 Results

3.3.1 Single-delay ASL

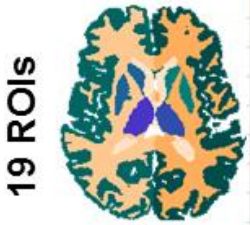

ROI analysis by 19 major tissue types

Index	Mask_name	Regional_CBF(ml/100g/min)	Regional_relative_CBF	Number_of_voxels
1	CerebralCortex_L	95.95	1.21	233157
2	CerebralCortex_R	104.82	1.32	243636
3	CerebralNucli_L	86.66	1.1	10556
4	CerebralNucli_R	88.21	1.11	11759
...	...			

ROI analysis by 54 major tissue types

Index	Mask_name	Regional_CBF(ml/100g/min)	Regional_relative_CBF	Number_of_voxels
1	Frontal_L	99.76	1.26	77277
2	Frontal_R	105.37	1.33	76926
3	Parietal_L	98.41	1.24	39856
4	Parietal_R	109.07	1.38	43660
...	...			

ROI analysis by 289major tissue types

Index	Mask_name	Regional_CBF(ml/100g/min)	Regional_relative_CBF	Number_of_voxels
1	SFG_L	101.3	1.28	9219
2	SFG_R	106.37	1.34	6653
3	SFG_PFC_L	91.52	1.16	8787
4	SFG_PFC_R	97.73	1.24	8621
5	SFG_pole_L	79.01	1	2310
6	SFG_pole_R	92.25	1.17	4070

Figure 3.5 Region-specific quantitative reports of ASL-derived parameters.
Three levels of brain parcellations (left panel) and their corresponding ROI-specific CBF values (right panel) are shown. Number of voxels within each parcellation are also included in the reports.

Figure 3.4 shows CBF maps generated from a representative single-delay ASL data set. The outcomes include absolute (in ml/100 g/min) and relative (with reference to whole-brain CBF) CBF maps in each of the following spaces: individual ASL space, individual T1 space, and MNI space. Figure 3.5a shows region-of-interest (ROI) results. Three levels of brain parcellations are provided, which divide the brain into 19, 54, and 289 ROIs, respectively. Figure 3.5b shows ROI CBF values as a function of age in a group of healthy subjects (N=309), demonstrating an age-related decline in brain perfusion which is consistent with findings in the literature (Chen et al 2011a, Lu et al 2011, Stoquart-ElSankari et al 2007).

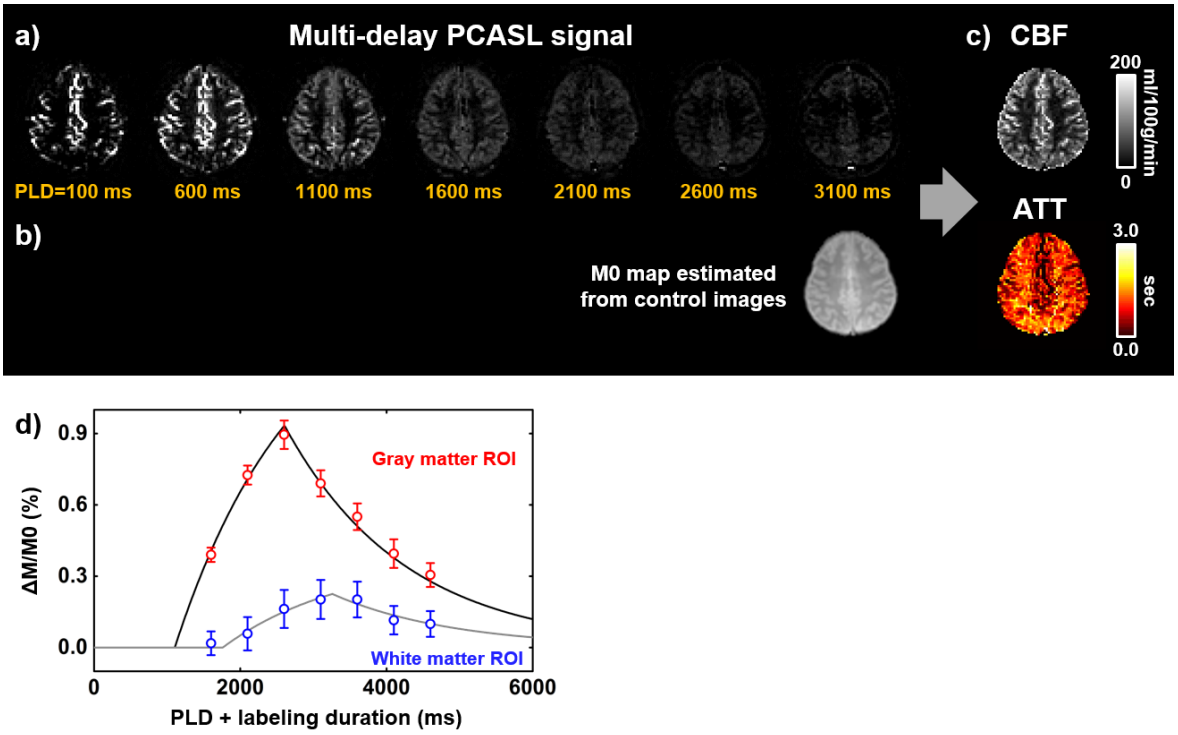

Figure 3.6 Multi-delay PCASL data processing.

The ASL images at a series of PLDs (a), the estimated M0 image (b), and their corresponding CBF and ATT maps (a) derived by ASL-MRICloud in multi-PLD PCASL. (d) The nonlinear curve fitting of signals from gray and white matter ROIs, respectively.

Additionally, the motion vectors are also provided in the outcome files. All outcomes of the ASL-MRICloud are downloadable through a .zip file.

3.3.2 Multi-delay ASL

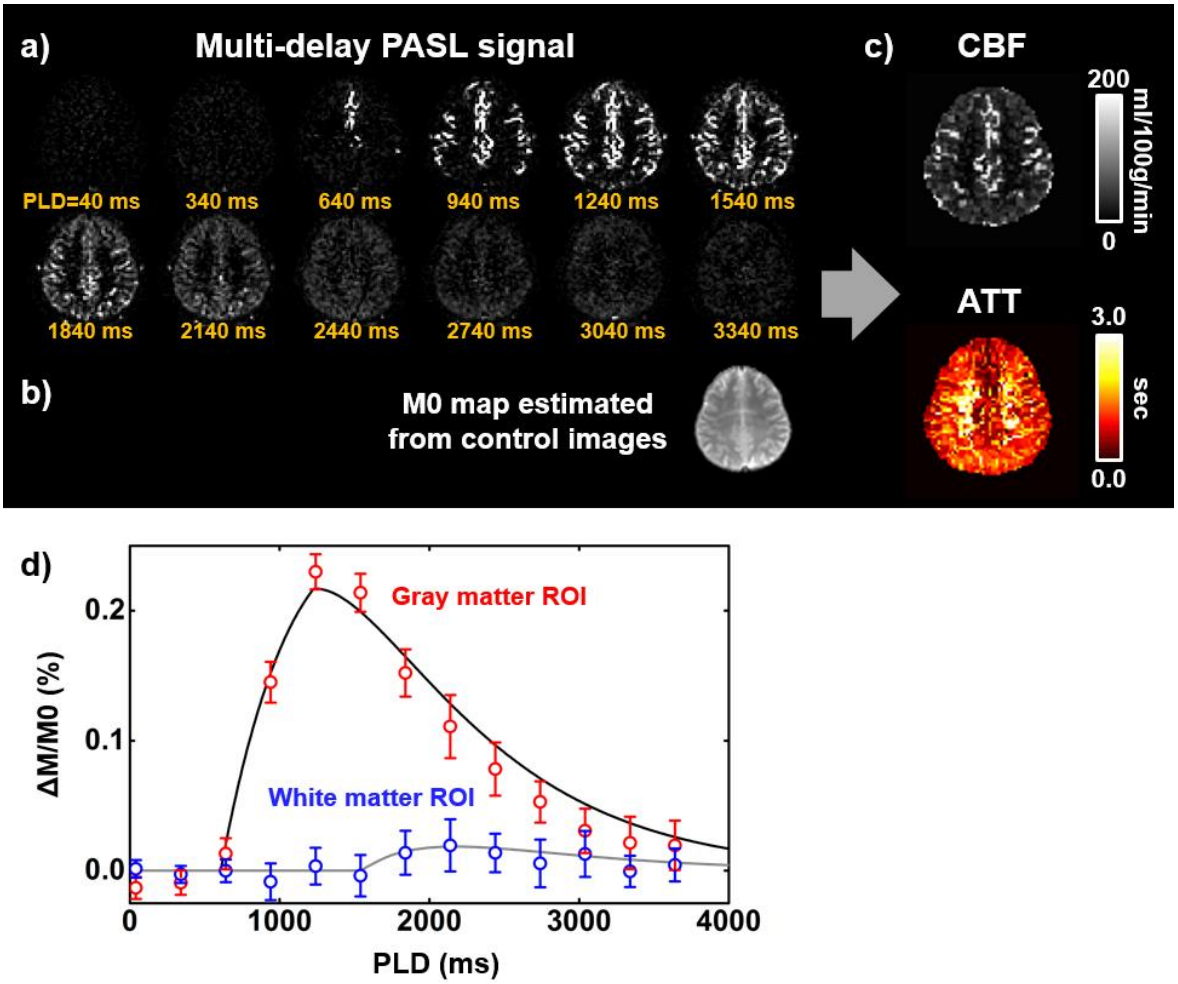

Figure 3.7 Multi-delay PASL (with Look-Locker acquisition) data processing.
The ASL images at a series of PLDs (a), the estimated M0 image (b), and their corresponding CBF and ATT maps (c) derived by ASL-MRICloud in multi-PLD PASL. (d) The nonlinear curve fitting of signals from gray and white matter ROIs, respectively.

A representative multi-delay PCASL data set is shown in Figure 3.6. Figure 3.6a shows difference images, i.e. control-label, as a function of PLD. Figure 3.6b displayed an M0 map that was obtained from fitting the control images to a saturation recovery curve. Figure 3.6c shows CBF and ATT maps from the kinetic model fitting. Figure 3.6d illustrates ROI results from a gray matter and a white matter ROI.

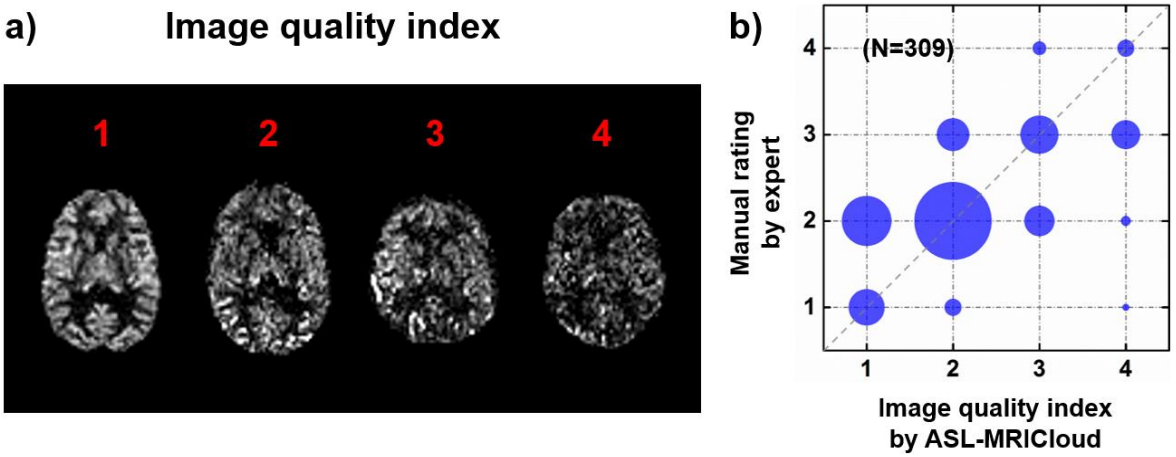

Figure 3.8 Examination assistance indices 1 - image quality index (QI).
(a) Four testing CBF maps with their corresponding QI score. (b) Scatter plot of manual ratings and QI on 309 ASL datasets (circle area is proportional to the number of datasets). QI was generated based on standard error of the voxel-wise CBF map across measurements.

Figure 3.7 shows a representative data set using multi-delay PASL.

3.3.3 Examination assistance indices

Figure 3.8a shows four representative CBF images, one for each QI category. It can be seen that, as the QI becomes larger, the quality of the CBF images is increasingly degraded. The QI can be used as a reference for the user to decide if the data set should be excluded from group analysis. We validated the QI by comparing it to manual ratings conducted by an experienced ASL researcher. Figure 3.8b shows a scatter plot between the automatic QI scales and the manual ratings. A strong correlation ($r = 0.82$) was observed.

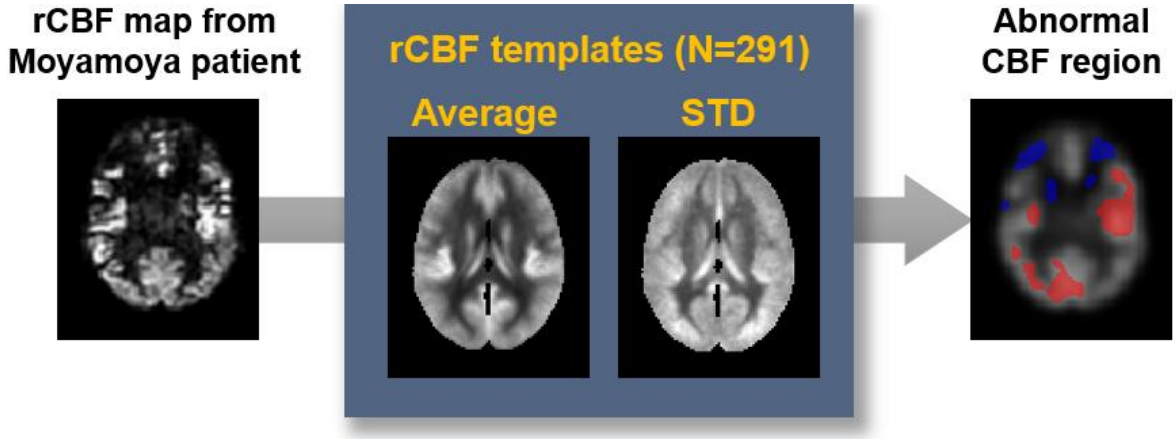

Figure 3.9 Examination assistance indices 2 – perfusion abnormality index.
Middle panel shows the mean and STD images of the 291 out of 309 relative CBF (rCBF) maps (that have manual rating < 4) from the database. After the rCBF map is generated from uploaded ASL data, its Z-score map is calculated based on these templates. The voxels with extra high/low Z-scores are detected, labeled as red/blue respectively. An rCBF map from a Moyamoya patient are shown for example.

Figure 3.9 shows an example of the Abnorm index map in a patient with Moyamoya disease, in whom both hypoperfusion (due to ischemia) and apparent hyperperfusion (due to delayed bolus clearance) are present.

3.4 Discussion

In this work, we developed ASL-MRICloud, a cloud-based tool for ASL data processing, which may be useful to the community in view of the increasing use of ASL in research and clinical settings. ASL-MRICloud employs a web interface for uploading data and downloading results, provides a fully automated analysis pipeline, and is capable of processing both single-delay and multi-delay ASL data.

3.4.1 Features of ASL-MRICloud

An important feature of the cloud-based analysis methods is that the user does not have to install the software on their local computer thus there is no burden on version or operating system compatibility. The tool also facilitates the dissemination of shared high-end computational resources, and the user does not have to be constrained by CPU and memory capacity of their own computer. In addition, the cloud-based analysis methods allow more efficient implementation of software updating and bug fixing. Finally, since the quantification of CBF is based on recommendations made in the ASL consensus paper, it can potentially promote standardization of ASL processing in the community.

Another useful feature associated with ASL-MRICloud is that this tool is closely integrated with other toolboxs on MRICloud, most notably the T1-MRICoud tool. The output from the T1 tool can thus be directly used by the ASL-MRICloud for registration purposes. The benefit of this integration is that CBF maps in the individual space can be automatically normalized into the MNI-space and that ROI CBF values will also be available. These outcome variables can then be readily used for study-specific statistical analyses.

To our knowledge, our group was among the first to implement cloud-based MRI processing tools in the community (Mori et al 2016, Shin et al 2016, Shin et al 2013). Since its conception in 2015, more than 6000 processing jobs have been submitted through MRICloud. For ASL-MRICloud, since this tool was launched in 2016, approximately 2000 jobs from outside our institution have been submitted and processed. Several research studies that used ASL-MRICloud has been published in scientific journals (De Vis et al 2018, Stephens et al 2018).

3.4.2 Comparison with other ASL processing software

Several other ASL processing programs have been developed. The ASL toolbox is a MATLAB-based script tool that is capable of providing CBF quantification, spatial normalization, and group analysis. In addition, the ASL toolbox is also featuring outlier elimination function, as well as cortex activation detection in functional ASL data. One downside with this package is that it requires functions from an additional MATLAB package SPM. Also, a large amount of basic MATLAB script programming and constant manual operation are necessary during processing ASL data. Another ASL processing package that runs in Linux system is BASIL, one of the toolbox from Functional Software Library (FSL) suite. BASIL is based on Bayesian inference principles and was primarily developed for multi-delay ASL data. The package also provides aid in CBF/ATT quantification and subsequent spatial processing, without relying on a MATLAB environment. But step-by-step and subject-by-subject processing is not evitable. In response, Automatic Software for ASL Processing (ASAP) was developed to support more automated processing procedures, with minimum user intervention. This MATLAB-based package wraps scripts into a user-friendly GUI and transforms the step-by-step calculation into button clicking. Nonetheless, a sizable amount of effort has to be made before using the GUI, such as setting up MATLAB environment with SPM. Besides the above toolboxes that provide a fairly comprehensive processing pipeline, several algorithms for step-specific optimizing are also proposed, such as Enhancement of Automated Blood Flow Estimates (ENABLE) for eliminating poor volumes of ASL signal, and Voxel-Wise Functional Connectomics for functional ASL denoising.

3.4.3 Protection of health information

Compared to ASL processing tools that are installed on local computers, ASL-MRICloud requires the user to upload their raw MRI data to a cloud server for processing. Thus, it is necessary that protected health information (PHI) is removed before uploading. In the current implementation, this requirement is met by using ANALYZE format in the file uploading. For users who only have DICOM files, we developed a converter software (written in C++) that removes the PHI from the DICOM data and save the de-identified data in ANALYZE file format. The drawback of this solution is that it adds an extra data conversion step to the user's workflow. Therefore, in future work, we will consider incorporating the anonymizing step in the main processing pipeline.

3.4.4 Limitations

One limitation of ASL-MRICloud is that it did not build in the flexibility for the user to adjust steps in the workflow. For example, some user may prefer some spatial smoothing of the data, but this is not feasible in the current implementation. We made this decision based on considerations of a tradeoff between flexibility and complexity. Another limitation is that there is an upper limit on the batch size, i.e. 10 data sets, the user can upload each time. This restriction was applied in consideration of the uploading size, preventing prolonged uploading time or upload abortion due to interrupted internet connection. Even with the current batch limit, we sometimes receive reports from our users that the time it takes to upload the data was excessive in certain part of the world. Therefore, we feel that a batch size of 10 is appropriate for our tool. For studies with large subject number, the user only needs to divide the data sets into several batches. A third potential limitation of ASL-MRICloud is that only the most common forms of ASL schemes were currently implemented. Future work will consider the inclusion of other promising ASL

sequeunces such as velocity selective ASL (Qin & van Zijl 2016, Wong et al 2006), Hadamard time-encoded ASL (Dai et al 2013, Teeuwisse et al 2014, Wells et al 2010), and MR fingerprinting ASL (Su et al 2017, Wright et al 2014).

3.5 Summary

We have developed an online processing tool for ASL MRI data, referred to as ASL-MRICloud. The tool is web-based and the processing is automatic. Use of the tool does not require installation of software on the local computer. We demonstrated that ASL-MRICloud can provide quantitative CBF maps in both individual and standard space as well as ROI CBF values in major brain structures. ASL-MRICloud may be a useful tool for ASL MRI data processing in clinical and research settings.

CHAPTER FOUR

4 Time-Resolved VASO CBV Imaging Facilitates Intracranial Vascular Compliance Mapping

4.1 Introduction

Vascular compliance (VC) represents the ability of a vessel to dilate or increase volume in response to an increase in blood pressure. This important property of vessel can convert the pulsatile flow in arteries to continuous flow into the capillaries, thus protects the vascular bed from disruptive pulsatile flow. A decreased vascular compliance has been regarded as a potentially important biomarker of a number of diseases, such as cardiovascular and cerebrovascular diseases, hypertension, diabetes, and Alzheimer's disease (Glasser et al 1997, Gorelick et al 2011, Laurent et al 2003, Zieman et al 2005). As a result, the vascular compliance measurement at major artery segments, including aorta, carotid, and femoral arteries, has already been proven to be of clinical significance (Laurent et al 2006, Van Bortel et al 2012). For example, it was reported that aortic stiffness can serve as an independent predictor of primary coronary events in a longitudinal study (Boutouyrie et al 2002).

Vascular compliance is traditionally measured with ultrasound (Oliver & Webb 2003). Echotracking techinique has been successful in detecting arterial diameter change due to pulsation of blood pressure, and the carotid-femoral pulse wave velocity (PWV) measured by ultrasound echotracking has been considered as the "gold-standard" measurement of arterial stiffness (Laurent et al 2006, Van Bortel et al 2012). The extended technique, transcranial Doppler ultrasound (TCD) has been applied to cerebral VC assessment (Aries et al 2010, Carrera et al 2011a). However, the TCD technique only measures the blood flow velocity change due to pulsation and lacks the capability to acquire the arterial geometry or blood volume, making it difficult to quantify the vascular compliance of intracranial arteries. ASL-based MRI methods were also proposed to assess arterial cerebral blood volume change in systole and diastole (Warnert et al 2015b, Yan et al 2016). But the quantification of CBV in those methods relies on complicated modeling and assumptions which may be prone to bias. The need for an effective methods to measure vascular compliance at intracranial arteries remains. Previously, vascular space-occupancy (VASO) technique was developed to detect brain stimulation induced CBV change in capillary bed (Lu et al 2003, Lu & van Zijl 2012), which has the potential to be adapted to measure arterial CBV (aCBV) change of larger arteries between systole and diastole.

The aim of this study is to develop a non-contrast MRI technique that allows the 3D vascular compliance mapping of intracranial arteries without using exogenous contrast agent. The technique utilized the cardiac pulsation as the intrinsic pressure stimuli and measured the induced aCBV change within a cardiac cycle based on the vascular space-occupancy (VASO) principle, from which VC is estimated. We termed the technique as time-resolved VASO MRI. This technique, when combined with 3D angiogram for display, allows visualization of vessel compliance map along the intracranial arterial tree. We conducted three experimental studies on

the time-resolved VASO technique. We first demonstrated the feasibility of the proposed method in measuring vascular compliance in the whole cerebral arterial tree. We also investigated its reproducibility across measurements. Finally, as a preliminary application, aging effect on VC results was evaluated in young and elderly subjects.

4.2 Methods

4.2.1 Pulse sequence

VASO technique was originally developed to assess CBV changes in response to brain activation (Lu et al 2003), in which the blood signal is selectively nulled and the local vasodilatation during stimulation is reflected in the decrease of tissue-only signal. Here the main idea is to measure aCBV changes within a cardiac cycle, which is presumably related to vascular compliance. To tailor the VASO technique for applications in intracranial arteries (as opposed to focusing on tissue as in fMRI studies), two changes were made to the conventional VASO sequence (Figure 4.1a). One was that the non-selective inversion was replaced by a 110° B1-insensive rotation pulse (BIR-4) (Garwood & DelaBarre 2001, Huber et al 2014), so that the blood-nulling point (TI_2 = 476 ms) is shorter and prevents fresh, uninverted spins to arrive at the arterial tree at the time of acquisition. The second modification was that a slab-selective inversion pulse (FOCI) (Warnking & Pike 2004) was placed at TI_1 = 2000 ms before the non-selective pulse to prepare the magnetization of CSF such that its signal is positive at the time of acquisition (see simulation results in Figure 4.1b). This way, regardless of whether the increase in CBV is accommodated by CSF or tissue volume reduction (or their combination), the VASO signal will always change in one direction (decreases when CBV increases).

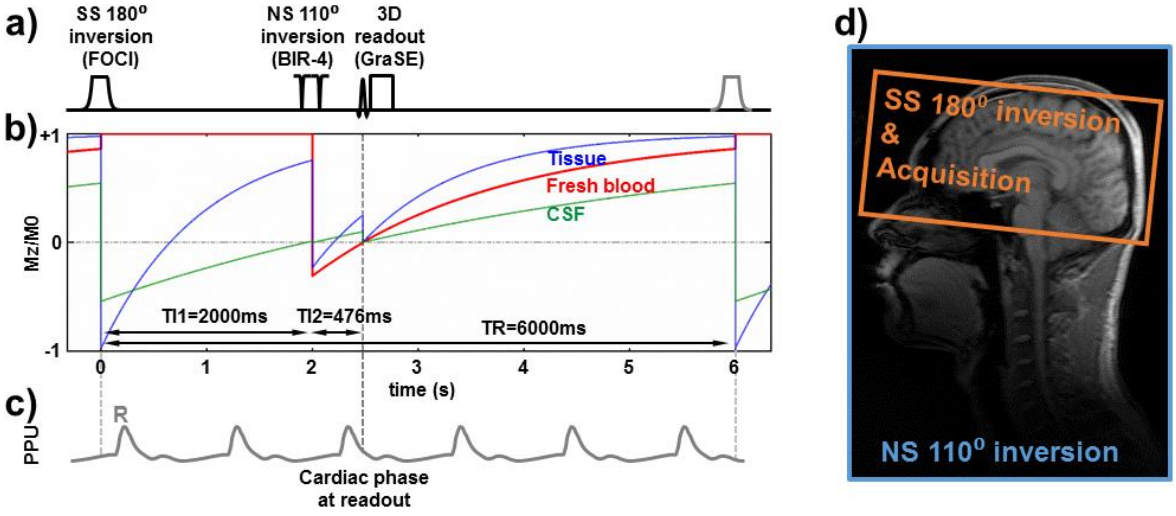

Figure 4.1 Sequence diagram and Bloch simulation of time-resolved VASO CBV imaging.

(a) The pulse sequence of proposed VASO, made up with two inversion pulses before acquisition. One is spatial-selective (SS) 180° FOCI that applied to the imaging slab; the other is non-selective (NS) 110° BIR-4. (b) Longitudinal magnetization of multiple compartments as a function of time. Red curve indicates fresh blood that fills into the arterial tree during TI_1, so it has full magnetization before second inversion pulse. (c) Pulsation curve recorded from the pulse device on the fingertip. (d) Geometric relationship between the first, second inversion pulse and imaging box.

4.2.2 Quantification of vascular compliance

The relative VASO signal difference between systolic and diastolic phases can be written as (Lu et al 2003),

$$\frac{\Delta S}{S} = \frac{S_{par}^{sys} - S_{par}^{dia}}{S_{par}^{dia}} = \frac{\left(C_{par} - aCBV^{sys} \cdot C_{blood}\right) - \left(C_{par} - aCBV^{dia} \cdot C_{blood}\right)}{C_{par} - aCBV^{dia} \cdot C_{blood}} = \frac{-\Delta aCBV \cdot C_{blood}}{C_{par} - aCBV^{dia} \cdot C_{blood}} \quad [6]$$

in which $C_{par\ (blood)}$ is the water density of tissue (blood) in mL water/mL tissue (blood), and $aCBV$ is defined as the percentage of blood volume within on imaging voxel. We assume that the vascular-space-occupancy within one voxel is less than 5% and thus $aCBV \ll 1$. Considering the value of the two constants, C_{par} = 0.89 mL water/mL tissue and C_{blood} = 0.85 mL water/mL blood (Lu et al 2002), are very close, we also assume $C_{par} = C_{blood}$ and the equation can be further simplified as,

$$\frac{\Delta S}{S} \approx -\Delta aCBV. \quad [7]$$

It can be seen that VASO signal change within a cardiac cycle is related to aCBV change. The vascular compliance index, VC, can then be written as,

$$VC = \frac{\Delta aCBV}{\Delta P} \approx \frac{|\Delta S|}{S \cdot \Delta P} \quad [8]$$

where ΔP is supposed to be carotid pulse pressure but we use pulse pressure measured at brachial as a substitute.

4.2.3 MRI experiments

The MRI experiment was carried out in a total of 11 healthy subjects (age 39.5±17.4 years, range 20–62, 5 males) using a 3T MRI scanner (Philips Healthcare, Best, the Netherlands). The RF transmission used the body coil, and the receiving coil was a 32-channel head coil. Foam padding was used to stabilize the head and minimize motion. The protocol was approved by local institutional review board. All subjects gave informed written consent before participating in the study. Three substudies were conducted to characterize different aspects of the technique, which are described separately in the following sections.

4.2.4 Feasibility study

Six young and healthy subjects (age 24.7±4.2 years, range 20-30 years, 1 male) participated in this substudy. The imaging parameters for VASO were as follows: the inversion time of FOCI selective-inversion pulse TI_1 = 2000 ms, the inversion time of BIR-4 global 110° inversion pulse TI_2 = 476 ms, TR = 6000 ms; single-shot 3D GRASE readout, field of view (FOV) = 180×180×104 mm^3, resolution = 4.5×4.5×8.0 mm^3, echo train length = 164 ms, Sensitivity encoding (SENSE) factor on phase encoding direction = 2.2; 100 dynamics, acquisition time = 10.3 min. To further ensure that the nulled blood has not left the major intracranial arteries after TI_2, we positioned the nose tip (instead of eyebrow) of the subject at the iso-center of B_0 field to achieve better B_0 homogeneity on lower neck and upper chest. Therefore, the blood in the extended region of common carotid/vertebral arteries could be effectively inverted by BIR-4 global 110° inversion pulse. A pulse oximeter (Invivo, Gainesville, FL) was attached to the index finger of the subject and the timing of cardiac pulse was recorded with reference to the pulse sequence timing

(specifically time of the excitation RF pulse) (see Figure 4.1c). This allows the investigation of the relationship between VASO signal intensity and cardiac phase.

To further confirm that the VASO signal change are indeed attributed to CBV pulsation, a cardiac-gated time-resolved phase-contrast (PC) MRI was performed to measure the blood flow velocity in the middle-cerebral-artery (MCA) as a function of cardiac phase. The signal from pulse device attached to the finger of the subject serves as the gating source. The following parameters were used: FOV = 200×200 mm^2, matrix = 400×400, FA = 15°, TE = 9.2 ms, VENC = 100 cm/s, 15 phases with an interval of 60 ms, a single coronal slice of 5-mm thickness at right MCA was imaged with a scan time of 6 min.

Finally, a 3D time-of-flight (TOF) angiogram was acquired to generate intracranial artery mask for display overlay. As such, the size, position, and angulation of FOV in TOF scan were identical with VASO to ensure exact spatial match between the two images. The imaging parameters for TOF MRI were as follows: 3D gradient-echo acquisition, axial slice orientation divided into 10 chunks, FOV = 180×180×104 mm^3, acquisition matrix = 376×240×208, voxel size = 0.48×0.75×0.5 mm^3, flip angle/TE/TR = 20°/3.45 ms/25 ms, SENSE factor = 2, scan duration = 7.5 min.

After the MRI scans and before the participant leave the scanner bed, brachial blood pressure (BP) was recorded while the participants were still in supine position, using a MR compatible cuff sphygmomanometer. Pulse pressure was calculated by subtracting the systolic and diastolic BP, and then used as a surrogate of intracranial pulse pressure to normalize the aCBV change. Note that the BP was not measure while sitting, because systolic/diastolic pressure is expected to elevate slightly in supine during MRI scan and the pulse pressure measured in sitting may not reflect the real blood pressure stimulation for CBV change while the scan.

4.2.5 Reproducibility study

Five healthy elderly subjects (age 57.2±4.6 years, range 52-62, 4 males) without significant systematic or neurologic disorders were scanned in this substudy. In addition to the scans that performed in feasibility study, the VASO scan was repeated one time within the session. The repetition allowed the assessment of coefficient-of-variation (CoV) across runs. Both Bland-Altman analysis between the two measurements were performed to evaluate the reproducibility of the technique.

4.2.6 Aging effect on intracranial vascular compliance

Aging is known to be the dominant condition that associated with increased arterial stiffness in major arteries, such as ascending/descending aorta, carotid artery, and femoral artery (Zieman et al 2005). In this study, we investigated the aging effect on intracranial vascular compliance by comparing the results of young and old groups from previous two substudies. Specifically, six young subjects (age 24.7±4.2 years) and five elderly subjects (age 57.2±4.6 years) were involved in this substudy. The pulse pressure change between the young and old was also examined.

4.2.7 Data analysis

The 100 images in VASO scan were motion corrected using SPM (University College London, London, UK) and then sorted by their corresponding cardiac phases. The cardiac phase at which the excitation RF pulse was played out was determined based on its location within the R-R interval and was written in radians (ranging from 0 to 2π) (Dagli et al 1999, Li et al 2018). For each voxel, its VASO signal intensity was plotted as a function of cardiac phase and then fitted

to a 2nd-order Fourier series (4 coefficients) (Dagli et al 1999). The difference between upper and lower peaks in the fitted curve gives the signal change between diastole and systole, ΔS. The average of the fitted curve gives the baseline tissue signal intensity, S. Therefore, voxel-by-voxel VC can be calculated accordingly by using Eq. 8, with the units of % voxel size per mmHg of blood pressure change.

To display the 3D VC map in a vessel-specific manner, the following three steps were performed to obtain an intracranial artery 3D model that encoded by VC value. First, the low-resolution VC map was resampled to the high-resolution TOF coordinates. Note that this procedure did not use interpolation, because we aimed to reserve the original VC value while interpolation may lower the VC value. Second, an intracranial artery mask was obtained by analyzing the TOF angiogram using the Amira software (FEI Visualization Sciences Group, Hillsboro, OR), and the voxels outside the artery mask were eliminated in the resampled VC map. Third, we used the Amira software to convert the masked VC map to a 3D surface model. Then the VC value was displayed on ParaView (Ayachit 2015) in vtk format.

The quantitative analysis of reproducibility and aging effect was achieved by calculating VC values in the level of region-of-interest (ROI). Six ROIs was drawn on the artery mask to encompass three major intracranial artery branches and three corresponding downstream bundles: anterior cerebral arteries (ACA), middle cerebral arteries (MCA), posterior cerebral arteries (PCA), and three smaller artery groups that fed by the three major arteries, respectively. The VC value of each ROI was then calculated by averaging the voxels of resampled VC map that located within the ROI mask.

4.3 Results

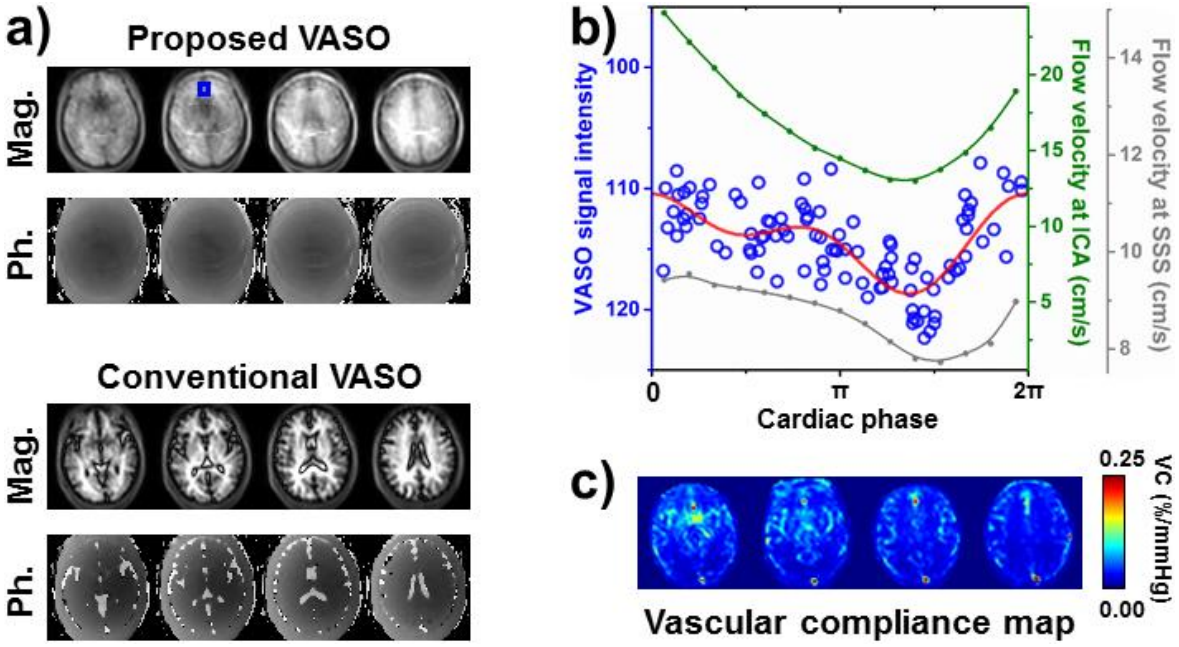

Figure 4.2 Representative results of time-resolved VASO technique.

(a) An example of proposed VASO images (magnitude and phase) acquired from one subject. Conventional VASO images are shown for comparison. (b) VASO signal intensity of one voxel (blue box in (a)) as a function of cardiac phase at acquisition. To show aCBV change intuitively, the scale of VASO signal is flipped upside-down considering its negative correlation with aCBV. Red curve represents the Fourier-series fitting. Gated phase-contrast derived flow velocity curves at ICA and SSS are overlaid. Minimum flow velocity and minimum aCBV appear at similar cardiac phase. (c) VC map generated from VASO image series.

4.3.1 Feasibility study

Figure 4.2a shows an example of proposed VASO images (including both magnitude and phase images). Note that both brain tissue signal and CSF signal are of same phase, as opposed to conventional VASO in which the CSF signal presents an opposite phase and counteract the signal

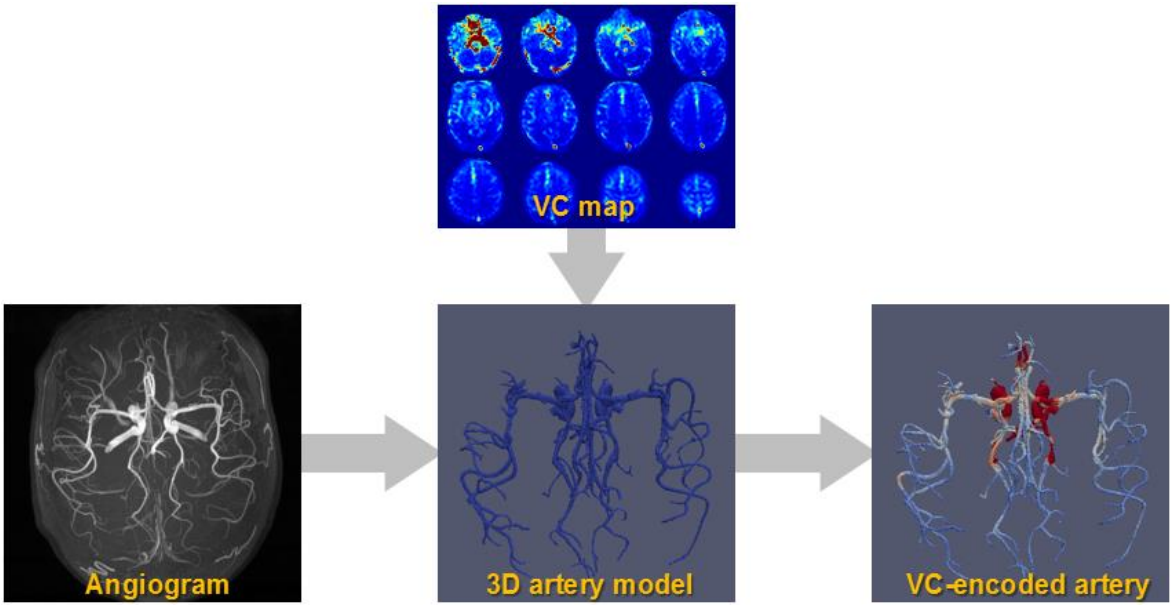

Figure 4.3 The workflow to generate VC-value-encoded 3D arterial trees from VASO and TOF angiography.

A 3D artery model is generated from TOF angiogram, followed by rendering VC map to the artery tree.

change in tissue. VASO signal as a function of cardiac phase (blue dots in Figure 4.2b) exhibits pronounced pulsatile modulation, suggesting an aCBV fluctuation introduced by cardiac pulsation. The source of the aCBV fluctuation is further confirmed by the fact that the timing pattern of aCBV fluctuation is consistent with that of CBF fluctuation, as can be seen in the cardiac-gated phase-contrast data (green curve in Figure 4.2b). Therefore, the aCBV change that induced by blood pressure change can then be quantified as vascular compliance. Figure 4.2c displays a voxel-by-voxel VC map. Large arteries, such as ACA, MCA, and PCA, reveal higher VC values than the smaller vessels. Interestingly, large vein, such as superior sagittal sinus (SSS), also shows high VC. Gated phase-contrast image suggested that large veins also have pulsatile flow (gray curve in Figure 4.2b).

To better visualize the results, VC map was rendered onto a 3D arterial tree structure that is generated from TOF angiogram (see Figure 4.3). Figure 4.4a shows the VC-value-encoded 3D arterial trees from three representative subjects. It can be seen that, as the vessel extends from trunk to branches, VC gradually decreases.

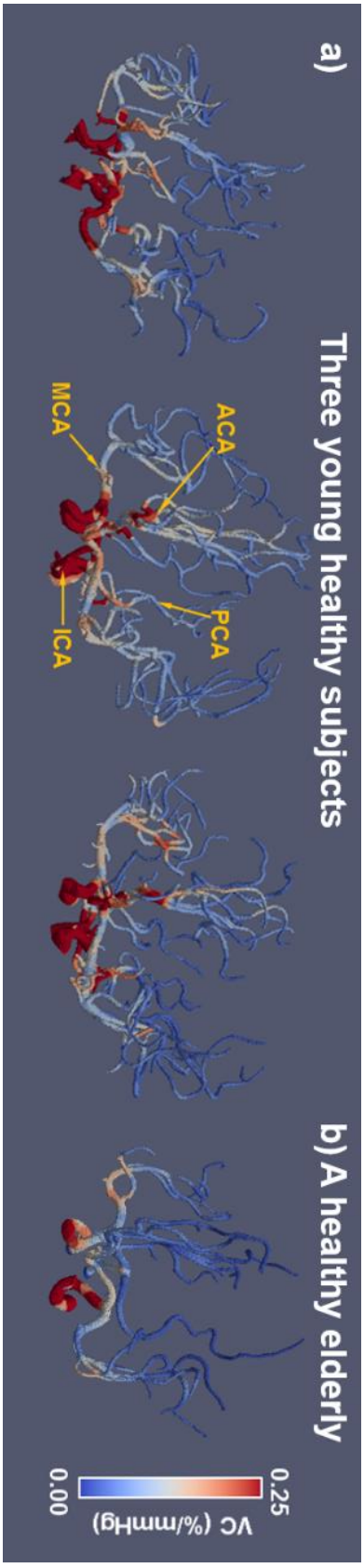
a)
Three young healthy subjects
MCA
ACA
PCA
ICA
b) A healthy elderly
0.00
0.25
VC (%/mmHg)

Figure 4.4 VC-value-encoded 3D arterial trees from three healthy young subjects (a), and one representative elderly subject (b).
Major arteries are labeled in the middle image.

4.3.2 Reproducibility study

Table 4.1summarizes the average value and the intra-session, inter-subject CoV for six region-of-interest of different artery structures. The six ROIs, of which three were major arteries and three were downstream smaller artery groups, are illustrated in Figure 4.5. It can be seen from Table 4.1 that the intra-session CoV, which reflects the measurement noise, is less than 5% for all six ROIs, suggesting high reliability of the techniques used. Figure 4.6a,b show a Bland-Altman plot and a scatter plot, respectively, between two VC measurements in the same session, again demonstrating a strong consistency across measurements ($r = 0.98$, $P < 10^{-5}$). For comparison, the inter-subject CoV in six ROIs are all more than 16%, much higher than intra-session CoV. Therefore, the VC measurement is capable to differentiate the VC variations between subjects.

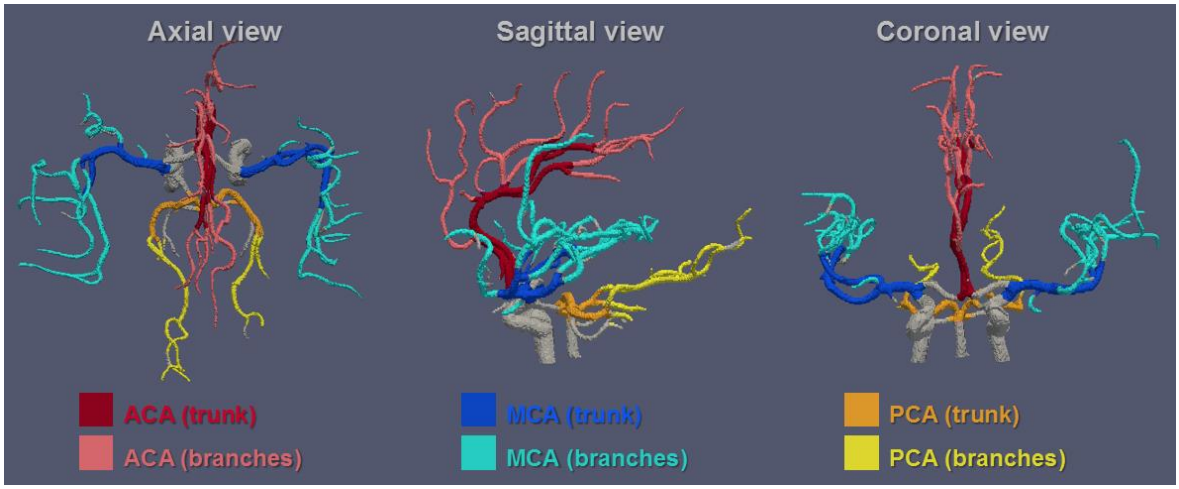

Figure 4.5 Region-of-interest overlaid on 3D model obtained from TOF.
The ROIs were drawn manually on the artery mask of each subject and the VC values were averaged within each ROI. The ROIs were used in both reproducibility and aging studies.

	VC (%/mmHg)	Intra-session CoV (%)	Inter-subject CoV (%)
ACA (trunk)	0.096 ± 0.024	4.1 ± 4.5	16.7
MCA (trunk)	0.098 ± 0.031	4.0 ± 2.9	22.6
PCA (trunk)	0.061 ± 0.014	4.7 ± 1.8	21.0
ACA (branches)	0.045 ± 0.008	4.0 ± 4.1	21.1
MCA (branches)	0.036 ± 0.006	2.8 ± 1.9	17.1
PCA (branches)	0.025 ± 0.006	3.5 ± 2.6	17.9

Table 4.1 Intra-session reproducibility of the VC measurements (Mean ± SD, N=5).

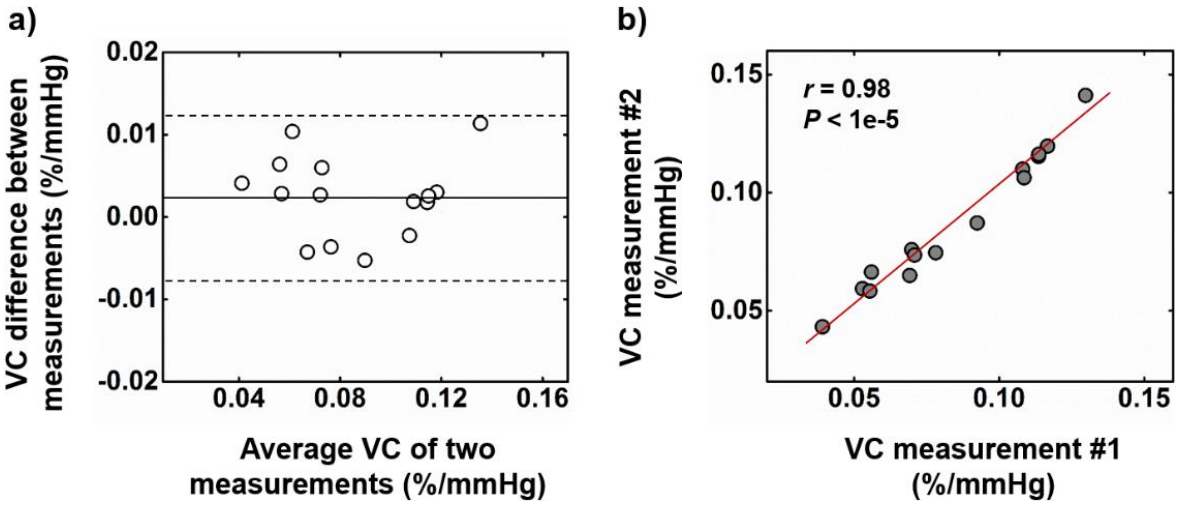

Figure 4.6 Intra-session reproducibility of the VC measurements (N=5).
VC values from three ROIs of large arteries (ACA, MCA, and PCA) were included in the analysis. (a) Bland–Altman plot comparing two VC measurements obtained within one session. The solid line indicates the mean difference between two measurements. The dashed lines indicate the 95% confidence interval. (b) Scatter plot of the two VC measurements. Each dot represents data from one session of one subject. The solid line indicates the linear regression curve (r = 0.98, $P < 10^{-5}$).

4.3.3 Aging effect on vascular compliance

An elevated brachial pulse pressure ($P = 0.02$) in elderly group (48.9±3.5 mmHg, N = 5) can be seen in Figure 4.7a, comparing with young group (38.2±1.9 mmHg, N = 6). One VC map from a representative elderly (age 62 years) is shown in Figure 4.4b, in which the vascular compliance value is visibly reduced across the whole arterial tree. The ROI comparisons are shown in Figure 4.7b and reveal two distinct features. One is that, consistent with visual appearance of VC maps in Figure 4.4, greater VC was observed in large arteries from both the young and elderly cohorts. The VC of smaller arteries show an overall 61.5% lower value as comparing with larger arteries across

all the subjects. The other feature is that the vascular compliance in elderly subjects decreased significantly ($P < 0.05$) in all six regions and on average by 46.8% in trunk arteries and by 36.6% in arteries branches, respectively.

4.4 Discussion

In this study, a novel MRI technique was presented for the quantitative mapping of intracranial vascular compliance without using exogenous contrast agent. The technique utilized the cardiac pulsation as the intrinsic pressure stimuli and measured the induced aCBV change within a cardiac cycle based on the vascular space-occupancy principle. We demonstrated that this technique was capable of measuring vascular compliance in the whole cerebral arterial tree and reveals that larger arteries are more compliant than small ones. The method was found to be reproducible with intra-session CoV of less than 5% across several region-of-interest. Finally, as a preliminary application, VC results of young and elderly subjects were compared and a substantially lower vascular compliance was detected in the elderly group. Clinical potentials

Vascular compliance, which reflects the stiffness of arterial vessel wall, serves as an important property of arteries to accommodate the pulsatile blood flow that originated from heart and smooth out the pulsatility into continuous in the capillary bed. The loss of vascular compliance of large arteries may expose the downstream arteriole and capillaries to strong blood pressure fluctuation, and as a consequence induces deterioration or damages to vessel walls. Arterial stiffness are now well accepted as an important biomarker of several disease states, including hypertension (Safar et al 2003), diabetes (Stehouwer et al 2008), cardiovascular disease (Mattace-Raso et al 2006), and a variety of cerebrovascular disease (e.g. stroke (Laurent et al 2003), small-

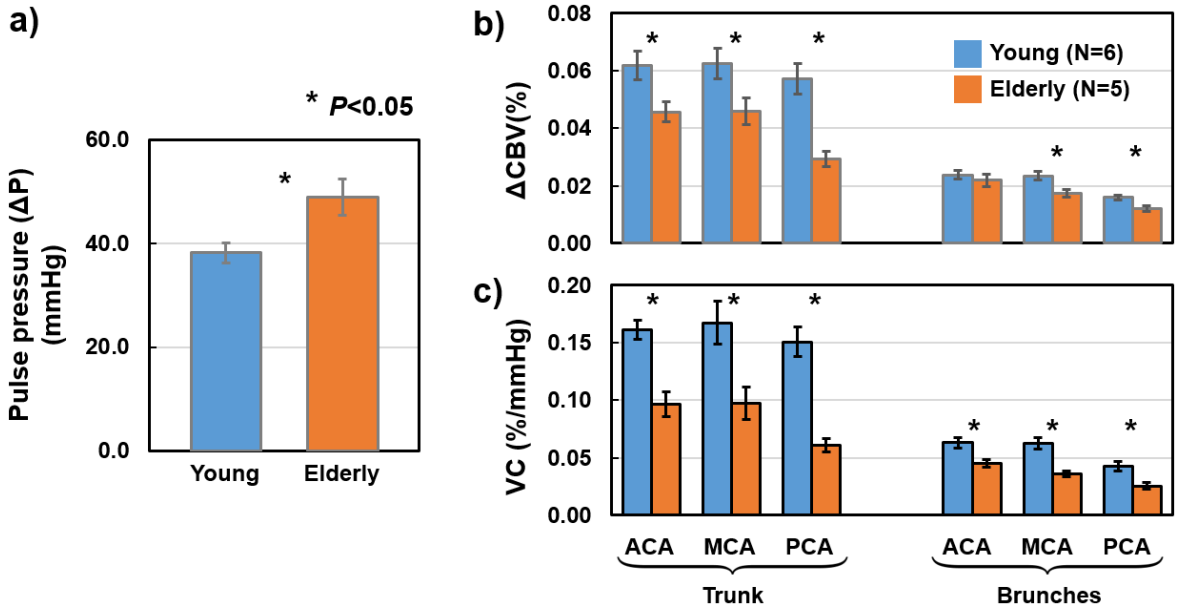

Figure 4.7 Aging effect on vascular compliance.

Aging effect on pulse pressure (a), CBV change during one cardiac cycle (b), and vascular compliance (c) between young (N=6) and elderly (N=5) subjects. Error bars indicate standard error.

vessel disease (Poels et al 2012a)). As a result, regional arterial stiffness along aortic, common carotid, common femoral, or brachial arteries, can be assessed in clinical settings by using primarily ultrasound echotracking method. However, the assessment of intracranial vascular compliance remains challenging due to lack of effective techniques. Therefore, the development of time-resolved VASO CBV imaging could potentially fill this gap and make it feasible to measure intracranial vascular compliance on a routine basis.

4.4.1 Comparison with other techniques

For the MR-based methods, the cross-sectional area of MCA in diastole and systole was directly imaged by cardiac-triggered T2-weighted sequence at 7 Tesla (Warnert et al 2016),

deriving only the distension of MCA but not VC due to no focal blood pressure measurement. Recently, two arterial-spin-labeling (ASL) based MRI techniques have been developed to estimate the aCBV change between systole and diastole. Yan et al. (Yan et al 2012, Yan et al 2016) demonstrated that by tracking the ASL signal time course with multi-phase bSSFP after pulsed spin labeling, one may quantify aCBV. Then the aCBV of systole or diastole can obtained when the multi-phase bSSFP ASL is triggered at corresponding cardiac phase. One shortcoming of this technique is that its single-slice acquisition manner limits the spatial coverage on the 3D extended arterial structure. It also requires an additional time-resolved PC to determine the trigger delay for the two cardiac phase. The other ASL-based method, reported by Warnert et al. (Warnert et al 2015b), estimates aCBV similarly by fitting a model of arterial input function to the multi-delay pulsed ASL data. The aCBV of diastole (systole) is thus obtained after binning the ASL data retrospectively to diastolic (systolic) phase. But this technique may result in unbalanced number of control and label images in each cardiac phase after retrospective synchronization, making it less efficient in data utilization. In contrast, the time-resolved VASO technique presented in this study is based on simple principle of blood nulling and does not rely on complicated modeling. The technique uses 3D acquisition and covers arteries of whole brain, allowing easy identification of ACA, MCA, and PCA. Furthermore, all the data were included into data processing despite of retrospective sorting on cardiac phase.

It should be noted that a direct comparison of intracranial VC reported here with VC values derived from ASL-based methods is not straightforward. The VC value in study of Warnert et al is normalized for the aCBV in diastole and therefore has the unit of percentage change in aCBV per mmHg (Warnert et al 2015b). While in the study of Yan et al., the derived VC value has the unit of mL per mmHg, but the CBV change accounts all the big arteries within the imaging slice

(Yan et al 2016). Nonetheless, Yan et al. found that VC decreases from big arteries to small arteries and old subjects tend to significantly lower VC comparing with young. It can be seen that the trend of VC results reported here is consistent with previous findings.

4.4.2 Technical considerations

The proposed VASO method in this study requires careful design of pulse sequence timing to ensure that, at the time of acquisition, all the blood in the artery tree are nulled and has not been substituted by inflow fresh blood. Meanwhile, the magnetization of CSF has to be kept in the same phase with tissue, otherwise CSF and tissue signal change may cancel out if an aCBV increase is accommodated by the reduction of both compartments. As such, two tailored pulses are included. First, a lower flip angle (i.e. 110°) instead of 180° was applied in front of acquisition to shorten the TI_2 for blood to recover to nulling point. This duration (476 ms) is less than the reported arterial arrival time ~1000 ms (Liu et al 2011). In addition, we chose the non-selective 110° to be adiabatic BIR-4 pulse such that the blood in the common carotid artery where has strong B_1/B_0 inhomogeneity are also effectively inverted (see Figure 4.8). Second, an adiabatic FOCI pulse selectively invert the tissue and CSF in the imaging FOV. After long TI_1, the CSF recovers to zero so it did not experience the BIR-4 110° and keep recovering. If not present, the magnetization of CSF with much longer T1 (~4500 ms) remains negative when tissue is already positive at the time of acquisition. The long TI_1 also provided sufficient time for the blood affected by the FOCI pulse in the FOV perfused to tissue, giving arterial space to fresh blood we want to null.

Note that a relatively large voxel size (4.5×4.5×8.0 mm^3) is used in the VASO acquisition, the reason is two folds: First, the quantification of VC using VASO signal change is based on the assumption that large artery CBV is less than 5% of the voxel size, and the large voxel size ensures

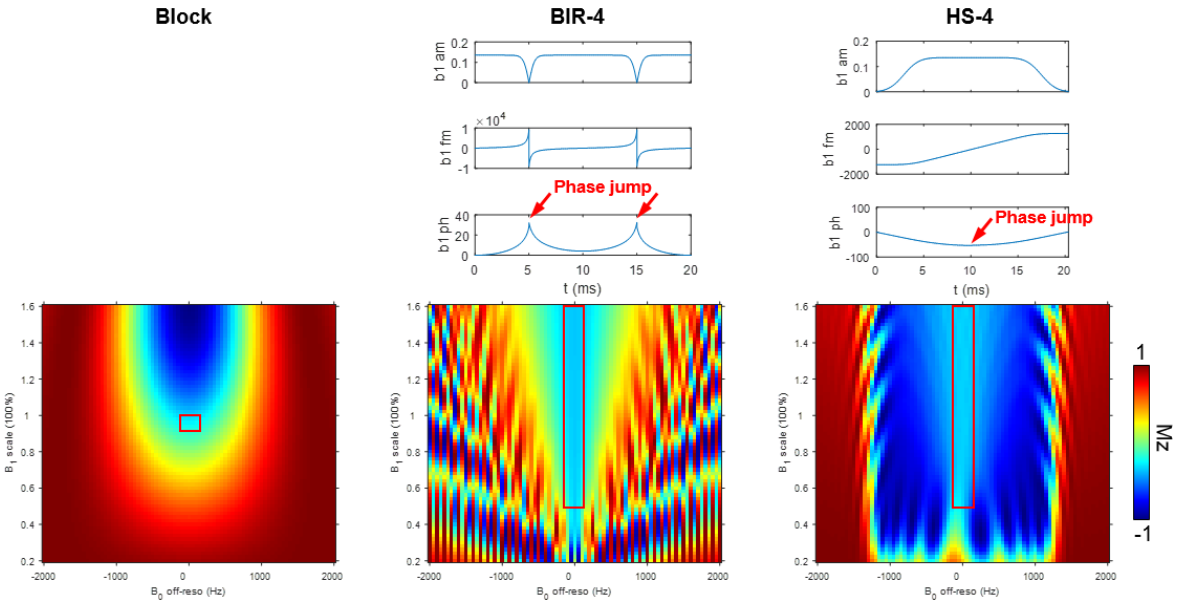

Figure 4.8 Bloch simulation of the 110° inversion pulse on its tolerance to B0/B1 inhomogeneity.

The red boxes in the bottom row represent targeted magnetization for the 110° inversion pulse. BIR-4 (Garwood & DelaBarre 2001) and HS-4 (Li et al 2017a) provide superior B1 tolerance comparing with simple block pulse. While a phantom study showed that HS-4 possess poor flipping homogeneity. Thus we selected BIR-4 as the non-selective 110° inversion pulse for our study.

the assumption is met; Second, a single-shot acquisition with short readout duration is preferred. Because the pulsation effect on aCBV may be smoothed out if the image is acquired with multiple shots or the readout extends to the whole cardiac cycle. At the same time, we still need to cover the whole brain. Thus, as a compromise, we acquired VASO images with large voxel size and low resolution.

This technique did not require cardiac triggering with ECG, which reduces burden to both MRI technologist and participant. Instead, a finger pulse device was used to record the pulsation timing with reference to RF excitation. The simple setup of the technique make it possible for

clinical routine. Also, unlike other retrospective method which has to abandon some of the data, the VASO images, regardless of at which cardiac phase the image was acquired, were all incorporated into the Fourier-series fitting to derive VC.

4.4.3 Limitations

One limitation of the VASO vascular compliance technique is that we used a global pulse pressure (i.e. brachial pulse pressure), instead of localized pulse pressure to normalize the CBV change across the arterial tree. The derived vascular compliance value could be underestimated in small arteries due to the fact that at the downstream of intracranial arterial tree, the pulse pressure was dampened. And to our knowledge, there is no method yet to measure the pulse pressure in a vessel-specific manner. This underestimation of vascular compliance value could be an intrinsic caveat of this time-resolved VASO CBV technique, as well as the ASL-based CBV imaging methods. Another drawback of the technique is that it could not provide the estimation of absolute aCBV at diastole to normalize the aCBV change. Therefore, the VC value measured here is dependent on voxel size. For example, same amount of aCBV change in a certain segment of MCA would appear as less percentage change in a large voxel than in a small voxel.

4.5 Summary

We demonstrated that arterial CBV fluctuation in a cardiac cycle can be quantified with a 3D VASO-MRI technique, the timing of which is consistent with CBF fluctuation. Such data can be used to map vascular compliance of intracranial arteries. We have proved its sensitivity in detecting vascular compliance alterations between young and elderly cohort. This method may

have potential utility in studies of cerebral arteriosclerosis, hypertension, diabetes, and related diseases.

CHAPTER FIVE

5 Conclusions and Future Direction

5.1 Conclusions

This thesis contributes three novel tools to improve the outcomes of brain perfusion imaging and vascular compliance imaging. We firstly identified and quantified the cardiac pulsation influence on the ASL perfusion imaging, and implemented cardiac-triggering scheme to significantly reduce the corresponding noise. Its utilities have been demonstrated in several experimental settings. Following the improvement on perfusion imaging technique, we built a cloud-based public-accessible tool to take over the acquired ASL data and performs the automated processing. Quantitative cerebral blood flow maps and region-specific reports are available for downloads within minutes. Finally, we extend our scope to investigate the larger cerebral arteries in term of vascular compliance. A time-resolved VASO technique was developed to offer 3D mapping of the whole cerebral artery tree and was applied to study aging effects on vascular compliance.

In the first aim, we report an intriguing and robust observation of pulsation modulation on the control/label signal in a PCASL protocol recommended by white paper. The source of the signal modulation was attributed to the pulsatile CBV change of intracranial arteries. The amount

of in-flow fresh blood spins that was not suppressed by BS varies accordingly with pulsatile CBV and therefore introduces signal fluctuation in both control and label series. As such, the SNR of PCASL was compromised even though several SNR-enhancing techniques have been applied, including BS and 3D acquisition. To increase the stability of ASL signal, we developed a cardiac-triggering based PCASL scheme that is capable of enhancing the temporal SNR by 94% in PCASL with single-shot 3D acquisition. We then tested the cardiac-triggering scheme in PCASL with multi-shot spiral TSE acquisition and achieved 22% decrease in CoV. The ring-shaped artifacts from pulsatile arteries were also reduced. We further evaluated the performance of cardiac-triggering in detecting CBF alterations using hypercapnia challenge as a model, and the results revealed similar CBF increase but noticeably less signal variance and artifacts comparing with that measured by regular PCASL. Additional analyses using the post-hoc correction methods revealed that CompCor and RETROICOR increased SNR of the regular PCASL data by 4.5±9.5% and 19.0±16.4%, respectively, in the whole-brain. But the extent of benefit was lower than that of the cardiac-triggered method.

In the second aim, we introduced ASL-MRICloud, a cloud-based tool for ASL data analysis, to accommodate the surging interest in ASL in research and clinical community. Compared with other existing ASL toolboxes that are based on local computing, ASL-MRICloud relies on a web interface for uploading data and downloading results, providing a fully automated interface to end users. The major innovation of the cloud-based analysis methods is that the user does not have to install any software on their local computer thus there is no worrying about version or operating system compatibility. The user also does not have to be constrained by CPU and memory capacity of their own computer, which can be a limiting factor in medical image analysis. In addition, the cloud-based analysis methods facilitate more efficient distribution of software updating or bug

fixing. The availability of the T1-based brain segmentation tool in MRICloud platform also allows region-specific quantitative reports of ASL-derived parameters as well as parametric maps normalization. To our knowledge, our group was among the first to implement a cloud-based ASL analysis tools in the community

In the third aim, a novel MRI technique was presented for the quantitative mapping of intracranial vascular compliance without using exogenous contrast agent. The technique utilized the cardiac pulsation as the intrinsic pressure stimuli and measured the induced aCBV change within a cardiac cycle based on the vascular space-occupancy principle. We demonstrated that this technique was capable of measuring vascular compliance in the whole cerebral arterial tree and reveals that larger arteries are more compliant than small ones. The method was found to be reproducible with intra-session CoV of less than 5% across several region-of-interest. Finally, as a preliminary application, VC results of young and elderly subjects were compared and a substantially lower vascular compliance was detected in the elderly group.

5.2 Future direction

Several additional steps are necessary to improve the utilities of the proposed tools in this thesis.

5.2.1 Integrating a camera-based cardiac-phase tracking system improves the convenience of performing cardiac-triggered PCASL.

The proper functioning of cardiac-triggered PCASL relies on the triggering signal from pulse oximeter attached to the finger of the patient. However, the patient must use the other hand to

move or scratch since movement of the hand that is attached to the placed pulse oximeter may interfere with accurate assessment of cardiac rate/pulse. Similarly, if the pulse oximeter falls off or loses signal due to hand movement, the scan may stall. To continue the scan, the operator would need to enter scanner room and adjust the pulse oximeter. Recently, a technique that features contact-free monitoring of human subjects to obtain cardiac and respiratory information was demonstrated to be feasible by using a small camera and light emitting diode (LED) mounted on the head coil of an MRI scanner (Maclaren et al 2015). The idea behind the technique is based on the fact that light absorption of the skin varies with the cardiac cycle. The researcher confirmed the cardiac-phase-dependent light absorption and proved that it is practical to obtain a useful signal in the MRI environment using simple hardware setup (i.e. a small camera and a LED in the head coil). This technique is an extension of previous work in adaptive motion correction, where small movements less than 0.1 mm in the head–foot direction show cardiac and respiratory motion (Maclaren et al 2012). With this monitoring technique implemented, the triggering signal can be extracted and the pulse oximeter is no longer needed. The setup of cardiac-triggered PCASL can be simplified accordingly.

5.2.2 Active update of ASL-MRICloud is necessary to keep pace with the fast development of ASL technology.

ASL-MRICloud only implemented the most common forms of ASL schemes, namely, single-delay PASL and PCASL, multi-delay PASL and PCASL. While other more advanced variations, such as velocity selective ASL (Qin & van Zijl 2016, Wong et al 2006), Hadamard time-encoded ASL (Teeuwisse et al 2014, von Samson-Himmelstjerna et al 2016), and MR fingerprinting ASL (Su et al 2017, Wright et al 2014), are absent due to the fact that those methods

are still under active development. These techniques represent new variants of ASL which offers higher acquisition efficiency and signal-to-noise ratio. It is necessary to follow up with the development of these methods and implement timely as soon as further validation has been performed. MRICloud.org provides a flexible platform for us to expand easily to include such methods as soon as these techniques mature and see more clinical applications.

5.2.3 Measuring localized pulse pressure in cerebral arteries increases the accuracy of vascular compliance quantification.

One potential systematic error that associated with VASO vascular compliance technique could arise from using brachial pulse pressure as a surrogate for intracranial pulse pressure. It has been reported that due to the pulse pressure amplification between central and peripheral arteries, it is inaccurate to use brachial pulse pressure as a surrogate for aortic or carotid pulse pressure, particularly in young subjects. In addition, a localized pulse pressure is required to normalize the CBV change of arterial tree so that vessel-specific vascular compliance value can be obtained. Otherwise, the derived vascular compliance value could be underestimated in small arteries due to the fact that at the downstream of intracranial arterial tree, the pulse pressure was dampened. At present, there still lacks a method to measure the pulse pressure in a vessel-specific manner. Preferably, a MR-based blood pressure technique could be developed in the future to fill the gap. An alternative solution may lie in the pulsatile blood flow measurement, in which pulsatile blood flow could be translated into pulse pressure by vessel fluid dynamic modeling (Ku 1997). Phase-contrast MRI has been utilized to measure the time-resolve 3D flow in aorta (Markl et al 2010) and could be a potential candidate for the proposed method.

BIBLIOGRAPHY

MRICloud website, braingps.mricloud.org.

Abad VM, Garcia-Polo P, O'Daly O, Hernandez-Tamames JA, Zelaya F. 2016. ASAP (Automatic Software for ASL Processing): A toolbox for processing Arterial Spin Labeling images. *Magn Reson Imaging* 34: 334-44

Alsop DC, Casement M, de Bazelaire C, Fong T, Press DZ. 2008. Hippocampal hyperperfusion in Alzheimer's disease. *Neuroimage* 42: 1267-74

Alsop DC, Detre JA. 1996. Reduced transit-time sensitivity in noninvasive magnetic resonance imaging of human cerebral blood flow. *J Cereb Blood Flow Metab* 16: 1236-49

Alsop DC, Detre JA, Golay X, Gunther M, Hendrikse J, et al. 2015. Recommended implementation of arterial spin-labeled perfusion MRI for clinical applications: A consensus of the ISMRM perfusion study group and the European consortium for ASL in dementia. *Magn Reson Med* 73: 102-16

Alsop DC, Detre JA, Grossman M. 2000. Assessment of cerebral blood flow in Alzheimer's disease by spin-labeled magnetic resonance imaging. *Ann Neurol* 47: 93-100

Aries MJ, Elting JW, De Keyser J, Kremer BP, Vroomen PC. 2010. Cerebral autoregulation in stroke: a review of transcranial Doppler studies. *Stroke* 41: 2697-704

Aslan S, Xu F, Wang PL, Uh J, Yezhuvath US, et al. 2010. Estimation of labeling efficiency in pseudocontinuous arterial spin labeling. *Magn Reson Med* 63: 765-71

Astrup J, Siesjo BK, Symon L. 1981. Thresholds in cerebral ischemia - the ischemic penumbra. *Stroke* 12: 723-5

Ayachit U. 2015. The ParaView guide: a parallel visualization application, pp. 276: Clifton Park, NY: Kitware Inc

Baron JC, Bousser MG, Rey A, Guillard A, Comar D, Castaigne P. 1981. Reversal of Focal Misery-Perfusion Syndrome by Extra-Intracranial Arterial Bypass in Hemodynamic Cerebral-Ischemia - a Case-Study with O-15 Positron Emission Tomography. *Stroke* 12: 454-59

Behzadi Y, Restom K, Liau J, Liu TT. 2007. A component based noise correction method (CompCor) for BOLD and perfusion based fMRI. *Neuroimage* 37: 90-101

Boutouyrie P, Tropeano AI, Asmar R, Gautier I, Benetos A, et al. 2002. Aortic stiffness is an independent predictor of primary coronary events in hypertensive patients - A longitudinal study. *Hypertension* 39: 10-15

Carrera E, Kim DJ, Castellani G, Zweifel C, Smielewski P, et al. 2011a. Cerebral arterial compliance in patients with internal carotid artery disease. *Eur J Neurol* 18: 711-8

Carrera E, Kim DJ, Castellani G, Zweifel C, Smielewski P, et al. 2011b. Cerebral arterial compliance in patients with internal carotid artery disease. *Eur J Neurol* 18: 711-18

Chalela JA, Alsop DC, Gonzalez-Atavales JB, Maldjian JA, Kasner SE, Detre JA. 2000a. Magnetic resonance perfusion imaging in acute ischemic stroke using continuous arterial spin labeling. *Stroke* 31: 680-87

Chalela JA, Alsop DC, Gonzalez-Atavales JB, Maldjian JA, Kasner SE, Detre JA. 2000b. Magnetic resonance perfusion imaging in acute ischemic stroke using continuous arterial spin labeling. *Stroke* 31: 680-7

Chappell MA, Groves AR, Whitcher B, Woolrich MW. 2009. Variational Bayesian Inference for a Nonlinear Forward Model. *Ieee T Signal Proces* 57: 223-36

Chen JJ, Rosas HD, Salat DH. 2011a. Age-associated reductions in cerebral blood flow are independent from regional atrophy. *Neuroimage* 55: 468-78

Chen Y, Wan HI, O'Reardon JP, Wang DJ, Wang Z, et al. 2011b. Quantification of cerebral blood flow as biomarker of drug effect: arterial spin labeling phMRI after a single dose of oral citalopram. *Clin Pharmacol Ther* 89: 251-8

Cheung N, Islam FMA, Jacobs DR, Sharrett AR, Klein R, et al. 2007. Arterial compliance and retinal vascular caliber in cerebrovascular disease. *Ann Neurol* 62: 618-24

Clark WM, Wissman S, Albers GW, Jhamandas JH, Madden KP, Hamilton S. 1999. Recombinant tissue-type plasminogen activator (Alteplase) for ischemic stroke 3 to 5 hours after symptom onset. The ATLANTIS Study: a randomized controlled trial. Alteplase Thrombolysis for Acute Noninterventional Therapy in Ischemic Stroke. *JAMA* 282: 2019-26

Coleman TF, Li YY. 1996. An interior trust region approach for nonlinear minimization subject to bounds. *Siam J Optimiz* 6: 418-45

Dagli MS, Ingeholm JE, Haxby JV. 1999. Localization of cardiac-induced signal change in fMRI. *Neuroimage* 9: 407-15

Dai W, Garcia D, de Bazelaire C, Alsop DC. 2008. Continuous flow-driven inversion for arterial spin labeling using pulsed radio frequency and gradient fields. *Magn Reson Med* 60: 1488-97

Dai WY, Shankaranarayanan A, Alsop DC. 2013. Volumetric measurement of perfusion and arterial transit delay using hadamard encoded continuous arterial spin labeling. *Magnetic Resonance in Medicine* 69: 1014-22

De Vis JB, Peng SL, Chen X, Li Y, Liu P, et al. 2018. Arterial-spin-labeling (ASL) perfusion MRI predicts cognitive function in elderly individuals: A 4-year longitudinal study. *J Magn Reson Imaging*

Detre JA, Leigh JS, Williams DS, Koretsky AP. 1992. Perfusion imaging. *Magn Reson Med* 23: 37-45

Donahue MJ, Faraco CC, Strother MK, Chappell MA, Rane S, et al. 2014. Bolus arrival time and cerebral blood flow responses to hypercarbia. *J Cereb Blood Flow Metab* 34: 1243-52

Fernandez-Seara MA, Aznarez-Sanado M, Mengual E, Irigoyen J, Heukamp F, Pastor MA. 2011. Effects on resting cerebral blood flow and functional connectivity induced by metoclopramide: a perfusion MRI study in healthy volunteers. *Br J Pharmacol* 163: 1639-52

Fernandez-Seara MA, Edlow BL, Hoang A, Wang J, Feinberg DA, Detre JA. 2008. Minimizing acquisition time of arterial spin labeling at 3T. *Magn Reson Med* 59: 1467-71

Fernandez-Seara MA, Wang Z, Wang J, Rao HY, Guenther M, et al. 2005. Continuous arterial spin labeling perfusion measurements using single shot 3D GRASE at 3 T. *Magn Reson Med* 54: 1241-7

Fushimi Y, Okada T, Yamamoto A, Kanagaki M, Fujimoto K, Togashi K. 2013. Timing dependence of peripheral pulse-wave-triggered pulsed arterial spin labeling. *NMR Biomed* 26: 1527-33

Gallagher D, Belmonte D, Deurenberg P, Wang Z, Krasnow N, et al. 1998. Organ-tissue mass measurement allows modeling of REE and metabolically active tissue mass. *Am J Physiol* 275: E249-58

Gamble G, Zorn J, Sanders G, Macmahon S, Sharpe N. 1994. Estimation of Arterial Stiffness, Compliance, and Distensibility from M-Mode Ultrasound Measurements of the Common Carotid-Artery. *Stroke* 25: 11-16

Garcia DM, Duhamel G, Alsop DC. 2005. Efficiency of inversion pulses for background suppressed arterial spin labeling. *Magn Reson Med* 54: 366-72

Gargiulo G, Tortora F, Cirillo M, Perrino C, Schiattarella GG, et al. 2013. Unexpected preserved brain perfusion imaging despite severe and diffuse atherosclerosis of supra-aortic trunks. *Cardiovasc J Afr* 24: e12-4

Garwood M, DelaBarre L. 2001. The return of the frequency sweep: Designing adiabatic pulses for contemporary NMR. *J Magn Reson* 153: 155-77

Gasser TC, Ogden RW, Holzapfel GA. 2006. Hyperelastic modelling of arterial layers with distributed collagen fibre orientations. *J R Soc Interface* 3: 15-35

Glasser SP, Arnett DK, McVeigh GE, Finkelstein SM, Bank AJ, et al. 1997. Vascular compliance and cardiovascular disease: a risk factor or a marker? *Am J Hypertens* 10: 1175-89

Glover GH, Li TQ, Ress D. 2000. Image-based method for retrospective correction of physiological motion effects in fMRI: RETROICOR. *Magn Reson Med* 44: 162-7

Gorelick PB, Scuteri A, Black SE, Decarli C, Greenberg SM, et al. 2011. Vascular contributions to cognitive impairment and dementia: a statement for healthcare professionals from the american heart association/american stroke association. *Stroke* 42: 2672-713

Greer JS, Wang X, Pedrosa I, Madhuranthakam AJ. 2016. Pulmonary Perfusion using pseudo-Continuous Arterial Spin Labeling. *Proc. Intl. Soc. Mag. Reson. Med.* 24: 2871

Gunther M, Oshio K, Feinberg DA. 2005. Single-shot 3D imaging techniques improve arterial spin labeling perfusion measurements. *Magn Reson Med* 54: 491-8

Hacke W, Kaste M, Bluhmki E, Brozman M, Davalos A, et al. 2008. Thrombolysis with alteplase 3 to 4.5 hours after acute ischemic stroke. *N Engl J Med* 359: 1317-29

Hademenos JG, Massoud T. 1998. *The Physics of Cerebrovascular Diseases : Biophysical Mechanisms of Development, Diagnosis and Therapy*. New York, United States: American Institute of Physics.

Hanon O, Haulon S, Lenoir H, Seux ML, Rigaud AS, et al. 2005. Relationship between arterial stiffness and cognitive function in elderly subjects with complaints of memory loss. *Stroke* 36: 2193-97

Heiss WD, Graf R. 1994. The Ischemic Penumbra. *Curr Opin Neurol* 7: 11-19

Henskens LHG, Kroon AA, van Oostenbrugge RJ, Gronenschild EHBM, Fuss-Lejeune MMJJ, et al. 2008. Increased Aortic Pulse Wave Velocity Is Associated With Silent Cerebral Small-Vessel Disease in Hypertensive Patients. *Hypertension* 52: 1120-U72

Hernandez-Garcia L, Jahanian H, Rowe DB. 2010. Quantitative analysis of arterial spin labeling FMRI data using a general linear model. *Magn Reson Imaging* 28: 919-27

Ho YC, Petersen ET, Zimine I, Golay X. 2011. Similarities and differences in arterial responses to hypercapnia and visual stimulation. *J Cereb Blood Flow Metab* 31: 560-71

Huber L, Ivanov D, Krieger SN, Streicher MN, Mildner T, et al. 2014. Slab-Selective, BOLD-Corrected VASO at 7 Tesla Provides Measures of Cerebral Blood Volume Reactivity with High Signal-to-Noise Ratio. *Magnet Reson Med* 72: 137-48

Jack CR, Bernstein MA, Fox NC, Thompson P, Alexander G, et al. 2008. The Alzheimer's Disease Neuroimaging Initiative (ADNI): MRI methods. *J Magn Reson Imaging* 27: 685-91

Jahanian H, Noll DC, Hernandez-Garcia L. 2011. B0 field inhomogeneity considerations in pseudo-continuous arterial spin labeling (pCASL): effects on tagging efficiency and correction strategy. *NMR Biomed* 24: 1202-9

Kalb RE, Helm TN, Sperry H, Thakral C, Abraham JL, Kanal E. 2008. Gadolinium-induced nephrogenic systemic fibrosis in a patient with an acute and transient kidney injury. *Brit J Dermatol* 158: 607-10

Kazan SM, Chappell MA, Payne SJ. 2010. Modelling the effects of cardiac pulsations in arterial spin labelling. *Phys Med Biol* 55: 799-816

Kim DJ, Kasprowicz M, Carrera E, Castellani G, Zweifel C, et al. 2009. The monitoring of relative changes in compartmental compliances of brain. *Physiol Meas* 30: 647-59

Ku DN. 1997. Blood flow in arteries. *Annu Rev Fluid Mech* 29: 399-434

Laurent S, Boutouyrie P, Lacolley P. 2005. Structural and genetic bases of arterial stiffness. *Hypertension* 45: 1050-55

Laurent S, Cockcroft J, Van Bortel L, Boutouyrie P, Giannattasio C, et al. 2006. Expert consensus document on arterial stiffness: methodological issues and clinical applications. *Eur Heart J* 27: 2588-605

Laurent S, Katsahian S, Fassot C, Tropeano AI, Gautier I, et al. 2003. Aortic stiffness is an independent predictor of fatal stroke in essential hypertension. *Stroke* 34: 1203-06

Lehmann ED, Hopkins KD, Rawesh A, Joseph RC, Kongola K, et al. 1998. Relation between number of cardiovascular risk factors/events and noninvasive Doppler ultrasound assessments of aortic compliance. *Hypertension* 32: 565-69

Li W, Griswold M, Yu X. 2010. Rapid T-1 Mapping of Mouse Myocardium With Saturation Recovery Look-Locker Method. *Magnetic Resonance in Medicine* 64: 1296-303

Li W, Liu P, Lu H, Strouse JJ, van Zijl PCM, Qin Q. 2017a. Fast measurement of blood T1 in the human carotid artery at 3T: Accuracy, precision, and reproducibility. *Magn Reson Med* 77: 2296-302

Li Y, Liu P, Li Y, Fan H, Peng SL, et al. 2017b. ASL-MRICloud: Towards a comprehensive online tool for ASL data analysis. *Proc. Intl. Soc. Mag. Reson. Med.* 25: 3808

Li Y, Mao D, Li Z, Schar M, Pillai JJ, et al. 2018. Cardiac-triggered pseudo-continuous arterial-spin-labeling: A cost-effective scheme to further enhance the reliability of arterial-spin-labeling MRI. *Magn Reson Med*

Li Z, Schar M, Wang D, Zwart NR, Madhuranthakam AJ, et al. 2016. Arterial spin labeled perfusion imaging using three-dimensional turbo spin echo with a distributed spiral-in/out trajectory. *Magn Reson Med* 75: 266-73

Liang X, Connelly A, Calamante F. 2015. Voxel-Wise Functional Connectomics Using Arterial Spin Labeling Functional Magnetic Resonance Imaging: The Role of Denoising. *Brain Connect* 5: 543-53

Liang X, Zou Q, He Y, Yang Y. 2013. Coupling of functional connectivity and regional cerebral blood flow reveals a physiological basis for network hubs of the human brain. *Proc Natl Acad Sci U S A* 110: 1929-34

Liu P, Li Y, Herrera A, Vasconcellos Faria VA, Ceritoglu C, et al. 2016. ASL in the MriCloud: a platform-independent, installation-free tool for arterial-spin-labeling analysis. *Proc. Intl. Soc. Mag. Reson. Med.* 24: 2877

Liu P, Uh J, Lu H. 2011. Determination of spin compartment in arterial spin labeling MRI. *Magn Reson Med* 65: 120-7

Lopez AD, Mathers CD, Ezzati M, Jamison DT, Murray CJ. 2006. Global and regional burden of disease and risk factors, 2001: systematic analysis of population health data. *Lancet* 367: 1747-57

Lu H, Golay X, Pekar JJ, van Zijl PCM. 2003. Functional magnetic resonance Imaging based on changes in vascular space occupancy. *Magnet Reson Med* 50: 263-74

Lu H, Golay X, van Zijl PC. 2002. Intervoxel heterogeneity of event-related functional magnetic resonance imaging responses as a function of T(1) weighting. *Neuroimage* 17: 943-55

Lu H, van Zijl PC. 2012. A review of the development of Vascular-Space-Occupancy (VASO) fMRI. *Neuroimage* 62: 736-42

Lu H, Xu F, Rodrigue KM, Kennedy KM, Cheng Y, et al. 2011. Alterations in cerebral metabolic rate and blood supply across the adult lifespan. *Cereb Cortex* 21: 1426-34

Maclaren J, Aksoy M, Bammer R. 2015. Contact-free physiological monitoring using a markerless optical system. *Magnetic Resonance in Medicine* 74: 571-77

Maclaren J, Armstrong BSR, Barrows RT, Danishad KA, Ernst T, et al. 2012. Measurement and Correction of Microscopic Head Motion during Magnetic Resonance Imaging of the Brain. *Plos One* 7

Markl M, Wallis W, Brendecke S, Simon J, Frydrychowicz A, Harloff A. 2010. Estimation of Global Aortic Pulse Wave Velocity by Flow-Sensitive 4D MRI. *Magnetic Resonance in Medicine* 63: 1575-82

Mattace-Raso FU, van der Cammen TJ, Hofman A, van Popele NM, Bos ML, et al. 2006. Arterial stiffness and risk of coronary heart disease and stroke: the Rotterdam Study. *Circulation* 113: 657-63

Miller KL, Alfaro-Almagro F, Bangerter NK, Thomas DL, Yacoub E, et al. 2016. Multimodal population brain imaging in the UK Biobank prospective epidemiological study. *Nat Neurosci* 19: 1523-36

Mori S, Wu D, Ceritoglu C, Li Y, Kolasny A, et al. 2016. MRICloud: Delivering High-Throughput MRI Neuroinformatics as Cloud-Based Software as a Service. *Comput Sci Eng* 18: 21-35

Mortality GBD, Causes of Death C. 2016. Global, regional, and national life expectancy, all-cause mortality, and cause-specific mortality for 249 causes of death, 1980-2015: a systematic analysis for the Global Burden of Disease Study 2015. *Lancet* 388: 1459-544

Mullan BA, Young IS, Fee H, McCance DR. 2002. Ascorbic acid reduces blood pressure and arterial stiffness in type 2 diabetes. *Hypertension* 40: 804-09

Oliver JJ, Webb DJ. 2003. Noninvasive assessment of arterial stiffness and risk of atherosclerotic events. *Arterioscler Thromb Vasc Biol* 23: 554-66

Orourke M. 1990. Arterial Stiffness, Systolic Blood-Pressure, and Logical Treatment of Arterial-Hypertension. *Hypertension* 15: 339-47

Pannier BM, Avolio AP, Hoeks A, Mancia G, Takazawa K. 2002. Methods and devices for measuring arterial compliance in humans. *Am J Hypertens* 15: 743-53

Poels MM, Zaccai K, Verwoert GC, Vernooij MW, Hofman A, et al. 2012a. Arterial stiffness and cerebral small vessel disease: the Rotterdam Scan Study. *Stroke* 43: 2637-42

Poels MMF, Zaccai K, Verwoert GC, Vernooij MW, Hofman A, et al. 2012b. Arterial Stiffness and Cerebral Small Vessel Disease The Rotterdam Scan Study. *Stroke* 43: 2637-+

Qin Q, van Zijl PC. 2016. Velocity-selective-inversion prepared arterial spin labeling. *Magn Reson Med* 76: 1136-48

Restom K, Behzadi Y, Liu TT. 2006. Physiological noise reduction for arterial spin labeling functional MRI. *Neuroimage* 31: 1104-15

Robson PM, Madhuranthakam AJ, Dai W, Pedrosa I, Rofsky NM, Alsop DC. 2009. Strategies for reducing respiratory motion artifacts in renal perfusion imaging with arterial spin labeling. *Magn Reson Med* 61: 1374-87

Rohl L, Ostergaard L, Simonsen CZ, Vestergaard-Poulsen P, Andersen G, et al. 2001. Viability thresholds of ischemic penumbra of hyperacute stroke defined by perfusion-weighted MRI and apparent diffusion coefficient. *Stroke* 32: 1140-6

Rusinek H, Brys M, Glodzik L, Switalski R, Tsui WH, et al. 2011. Hippocampal blood flow in normal aging measured with arterial spin labeling at 3T. *Magn Reson Med* 65: 128-37

Safar ME, Levy BI, Struijker-Boudier H. 2003. Current perspectives on arterial stiffness and pulse pressure in hypertension and cardiovascular diseases. *Circulation* 107: 2864-9

Schlaug G, Benfield A, Baird AE, Siewert B, Lovblad KO, et al. 1999. The ischemic penumbra: operationally defined by diffusion and perfusion MRI. *Neurology* 53: 1528-37

Shin DD, Ozyurt IB, Brown GG, Fennema-Notestine C, Liu TT. 2016. The Cerebral Blood Flow Biomedical Informatics Research Network (CBFBIRN) data repository. *Neuroimage* 124: 1202-7

Shin DD, Ozyurt IB, Liu TT. 2013. The Cerebral Blood Flow Biomedical Informatics Research Network (CBFBIRN) database and analysis pipeline for arterial spin labeling MRI data. *Front Neuroinform* 7: 21

Shin WY, Gu H, Yang YH. 2009. Fast High-Resolution T-1 Mapping Using Inversion-Recovery Look-Locker Echo-Planar Imaging at Steady State: Optimization for Accuracy and Reliability. *Magnetic Resonance in Medicine* 61: 899-906

Shirzadi Z, Crane DE, Robertson AD, Maralani PJ, Aviv RI, et al. 2015. Automated removal of spurious intermediate cerebral blood flow volumes improves image quality among older patients: A clinical arterial spin labeling investigation. *J Magn Reson Imaging* 42: 1377-85

Sobesky J, Zaro-Weber O, Lehnhardt FG, V H, Neveling M, et al. 2005. Does the mismatch match the penumbra? Magnetic resonance imaging and positron emission tomography in early ischemic stroke. *Stroke* 36: 980-85

Stehouwer CD, Henry RM, Ferreira I. 2008. Arterial stiffness in diabetes and the metabolic syndrome: a pathway to cardiovascular disease. *Diabetologia* 51: 527-39

Stephens JA, Liu PY, Lu HZ, Suskauer SJ. 2018. Cerebral Blood Flow after Mild Traumatic Brain Injury: Associations between Symptoms and Post-Injury Perfusion. *J Neurotraum* 35: 241-48

Stoquart-ElSankari S, Baledent O, Gondry-Jouet C, Makki M, Godefroy O, Meyer ME. 2007. Aging effects on cerebral blood and cerebrospinal fluid flows. *J Cereb Blood Flow Metab* 27: 1563-72

Su P, Mao D, Liu P, Li Y, Pinho MC, et al. 2016. Multiparametric estimation of brain hemodynamics with MR fingerprinting ASL. *Magn Reson Med*

Su P, Mao D, Liu PY, Li Y, Pinho MC, et al. 2017. Multiparametric Estimation of Brain Hemodynamics With MR Fingerprinting ASL. *Magnetic Resonance in Medicine* 78: 1812-23

Tanaka H, Dinenno FA, Monahan KD, Clevenger CM, DeSouza CA, Seals DR. 2000. Aging, habitual exercise, and dynamic arterial compliance. *Circulation* 102: 1270-5

Tarumi T, Ayaz Khan M, Liu J, Tseng BY, Parker R, et al. 2014. Cerebral hemodynamics in normal aging: central artery stiffness, wave reflection, and pressure pulsatility. *J Cereb Blood Flow Metab* 34: 971-8

Teeuwisse WM, Schmid S, Ghariq E, Veer IM, van Osch MJ. 2014. Time-encoded pseudocontinuous arterial spin labeling: basic properties and timing strategies for human applications. *Magn Reson Med* 72: 1712-22

Thomas FC, Li YY. 1994. On the Convergence of Interior-Reflective Newton Methods for Nonlinear Minimization Subject to Bounds. *Math Program* 67: 189-224

Turley DC, Pipe JG. 2013. Distributed spirals: a new class of three-dimensional k-space trajectories. *Magn Reson Med* 70: 413-9

Van Bortel LM, Laurent S, Boutouyrie P, Chowienczyk P, Cruickshank JK, et al. 2012. Expert consensus document on the measurement of aortic stiffness in daily practice using carotid-femoral pulse wave velocity. *J Hypertens* 30: 445-48

van der Worp HB, van Gijn J. 2007. Acute ischemic stroke. *New Engl J Med* 357: 572-79

Verbree J, van Osch MJ. 2017. Influence of the cardiac cycle on pCASL: cardiac triggering of the end-of-labeling. *MAGMA*

von Samson-Himmelstjerna F, Madai VI, Sobesky J, Guenther M. 2016. Walsh-ordered hadamard time-encoded pseudocontinuous ASL (WH pCASL). *Magn Reson Med* 76: 1814-24

Wang Z, Aguirre GK, Rao H, Wang J, Fernandez-Seara MA, et al. 2008. Empirical optimization of ASL data analysis using an ASL data processing toolbox: ASLtbx. *Magn Reson Imaging* 26: 261-69

Warnert EA, Murphy K, Hall JE, Wise RG. 2015a. Noninvasive assessment of arterial compliance of human cerebral arteries with short inversion time arterial spin labeling. *J Cereb Blood Flow Metab* 35: 461-8

Warnert EAH, Murphy K, Hall JE, Wise RG. 2015b. Noninvasive assessment of arterial compliance of human cerebral arteries with short inversion time arterial spin labeling. *J Cerebr Blood F Met* 35: 461-68

Warnert EAH, Verbree J, Wise RG, van Osch MJP. 2016. Using High-Field Magnetic Resonance Imaging to Estimate Distensibility of the Middle Cerebral Artery. *Neurodegener Dis* 16: 407-10

Warnking JM, Pike GB. 2004. Bandwidth-modulated adiabatic RF pulses for uniform selective saturation and inversion. *Magn Reson Med* 52: 1190-9

Wells JA, Lythgoe MF, Gadian DG, Ordidge RJ, Thomas DL. 2010. In vivo Hadamard encoded continuous arterial spin labeling (H-CASL). *Magn Reson Med* 63: 1111-8

Williams DS, Detre JA, Leigh JS, Koretsky AP. 1992. Magnetic-Resonance-Imaging of Perfusion Using Spin Inversion of Arterial Water. *P Natl Acad Sci USA* 89: 212-16

Wintermark M, Sesay M, Barbier E, Borbely K, Dillon WP, et al. 2005. Comparative overview of brain perfusion imaging techniques. *J Neuroradiology* 32: 294-314

Wong EC, Cronin M, Wu WC, Inglis B, Frank LR, Liu TT. 2006. Velocity-selective arterial spin labeling. *Magn Reson Med* 55: 1334-41

Wright LK, Ma D, Jiang Y, Gulani V, Griswold AM, Hernandez-Garcia L. 2014. Theoretical framework for MR fingerprinting with ASL: simultaneous quantification of CBF, transit time, and T1. *Proc. Intl. Soc. Mag. Reson. Med.* 22: 0417

Wu WC, Edlow BL, Elliot MA, Wang J, Detre JA. 2009. Physiological modulations in arterial spin labeling perfusion magnetic resonance imaging. *IEEE Trans Med Imaging* 28: 703-9

Wu WC, Fernandez-Seara M, Detre JA, Wehrli FW, Wang J. 2007a. A theoretical and experimental investigation of the tagging efficiency of pseudocontinuous arterial spin labeling. *Magn Reson Med* 58: 1020-7

Wu WC, Mazaheri Y, Wong EC. 2007b. The effects of flow dispersion and cardiac pulsation in arterial spin labeling. *IEEE Trans Med Imaging* 26: 84-92

Xu F, Uh J, Brier MR, Hart J, Jr., Yezhuvath US, et al. 2011. The influence of carbon dioxide on brain activity and metabolism in conscious humans. *J Cereb Blood Flow Metab* 31: 58-67

Yan LR, Li C, Kilroy E, Wehrli FW, Wang DJJ. 2012. Quantification of arterial cerebral blood volume using multiphase-balanced SSFP-based ASL. *Magnet Reson Med* 68: 130-39

Yan LR, Liu CY, Smith RX, Jog M, Langham M, et al. 2016. Assessing intracranial vascular compliance using dynamic arterial spin labeling. *Neuroimage* 124: 433-41

Ye FQ, Frank JA, Weinberger DR, McLaughlin AC. 2000. Noise reduction in 3D perfusion imaging by attenuating the static signal in arterial spin tagging (ASSIST). *Magn Reson Med* 44: 92-100

Ye FQ, Mattay VS, Jezzard P, Frank JA, Weinberger DR, McLaughlin AC. 1997. Correction for vascular artifacts in cerebral blood flow values measured by using arterial spin tagging techniques. *Magn Reson Med* 37: 226-35

Young WL. 1997. Physiology of the cerebral circulation. *Dev C C Med* 32: 1-16

Zaharchuk G, Do HM, Marks MP, Rosenberg J, Moseley ME, Steinberg GK. 2011. Arterial spin-labeling MRI can identify the presence and intensity of collateral perfusion in patients with moyamoya disease. *Stroke* 42: 2485-91

Zaharchuk G, El Mogy IS, Fischbein NJ, Albers GW. 2012a. Comparison of arterial spin labeling and bolus perfusion-weighted imaging for detecting mismatch in acute stroke. *Stroke* 43: 1843-8

Zaharchuk G, Olivot JM, Fischbein NJ, Bammer R, Straka M, et al. 2012b. Arterial Spin Labeling Imaging Findings in Transient Ischemic Attack Patients: Comparison with Diffusion- and Bolus Perfusion-Weighted Imaging. *Cerebrovasc Dis* 34: 221-28

Zebekakis PE, Nawrot T, Thijs L, Balkestein EJ, van der Heijden-Spek J, et al. 2005. Obesity is associated with increased arterial stiffness from adolescence until old age. *J Hypertens* 23: 1839-46

Zieman SJ, Melenovsky V, Kass DA. 2005. Mechanisms, pathophysiology, and therapy of arterial stiffness. *Arterioscler Thromb Vasc Biol* 25: 932-43

Zwart NR, Pipe JG. 2015. Graphical programming interface: A development environment for MRI methods. *Magn Reson Med* 74: 1449-60